arXiv:2105.06989v4 [cond-mat.quant-gas] 15 Feb 2022

Phase Space Crystal Vibrations: Chiral Edge States with Preserved Time-reversal Symmetry

Lingzhen Guo,[1,2] Vittorio Peano,[1] and Florian Marquardt[1,3]

[1] *Max Planck Institute for the Science of Light, Staudtstrasse 2, 91058 Erlangen, Germany*
[2] *School of Science, Nanjing University of Science and Technology, Nanjing 210094, China*
[3] *Physics Department, University of Erlangen-Nuremberg, Staudtstrasse 5, 91058 Erlangen, Germany*

(Dated: February 16, 2022)

It was recently discovered that atoms subject to a time-periodic drive can give rise to a crystal structure in phase space. In this work, we point out the atom-atom interactions give rise to collective phonon excitations of phase space crystal via a pairing interaction with intrinsically complex phases that can lead to a phononic Chern insulator, accompanied by topologically robust chiral transport along the edge of the phase space crystal. This topological phase is realized even in scenarios where the time-reversal transformation is a symmetry, which is surprising because the breaking of time-reversal symmetry is a strict precondition for topological chiral transport in the standard setting of real space crystals. Our work has also important implications for the dynamics of 2D charged particles in a strong magnetic field.

I. INTRODUCTION

The quantum Hall current in a two-dimensional (2D) electron gas pierced by a magnetic flux is insensitive to weak disorder, because it is carried by chiral edge states that do not have a counter-propagating counterpart[1,2]. With the proposal of the quantum anomalous Hall effect (QAHE)[3], Haldane showed that the key ingredient to engineer chiral edge states is not a net magnetic field flux, but rather the breaking of the time-reversal symmetry (TRS) itself. This insight has opened the way to the current focus on topological transport of neutral excitations such as photons[4–6], magnons[7,8], phonons[9,10] and cold atoms[11,12].

In this work, we introduce a conceptually different way to generate robust chiral phonon transport, without requiring a breaking of the TRS. A *single quantum* particle moving on a closed path in phase space acquires a Berry phase[13–16]. Therefore, when one considers the quantum motion in an extended periodic phase-space potential, the resulting matter wave bandstructure supports non-trivial Chern numbers[15,17,18]. However, so far it was unclear how this could lead to the most important consequence of such Chern numbers, namely chiral edge channels, since it is not straightforward to produce a boundary of such a phase-space potential. Here we consider a different scenario, demonstrating a new mechanism that occurs already in the *classical* domain, but only if one considers an *interacting many-particle* system. When the particles arrange themselves in the extrema of the underlying phase-space potential, it gives rise to a so-called phase space crystal[15]. We will show that the phase-space crystal vibrations acquire a topologically non-trivial band structure, due to the combination of interactions and symplectic phase-space geometry. In contrast to the single-particle case, the boundary of the finitely extended phase space crystal naturally supports chiral edge channels in phase space, which are now of phononic (collective) nature. We show that these chiral edge channels can arise even when the driving preserves the time-reversal symmetry. Finally, we explore the implications of our work for the crystal phase of 2D charged particles confined in the Lowest Landau Level (LLL) in the presence of a strong magnetic field.

Similar to Floquet approaches for topology[19,20], we will be employing time-dependent driving, but in our case the drive itself need not break TRS to generate chiral transport, as a consequence of the nonlocal nature of the time reversal operation in phase space. Our construction produces topological channels in a 2D phase space, starting from 1D real space. This is reminiscent of synthetic dimensions[21–23], but unlike that concept, no extra controlled degree of freedom is needed, we automatically get chiral motion, and besides in synthetic dimensions it is very challenging to create non-trivial lattice structures[24] or local and isotropic interactions[22], in contrast to the present approach.

The remaining part of this paper is organised as follows. In Sec. II, we introduce a model for a kicked harmonic oscillator. Our model allows to engineer any arbitrary lattice Hamiltonian in phase space by selecting an appropriate kicking sequence. We present the time-reversal-invariant kicking sequence that generates a honeycomb lattice Hamiltonian in phase space. In Sec. III, we investigate the atom-atom interactions for an ensemble of atoms confined in our phase-space lattice. Starting from the full phase-space many-body Hamiltonian, we derive an effective quadratic Hamiltonian for the small vibrations about a phase-space crystal equilibrium configuration. In Sec. IV, we study the resulting bulk band structure and show that it supports a topological band gap with a non-zero Chern number, even though our model is symmetric under time reversal transformation. In Sec. V, we investigate the phase space crystal vibrations in the presence of physical boundaries. We compare our phase-space Chern insulator with standard real space Chern insulators and explain why the breaking of the time-reversal symmetry is not a precondition for robust

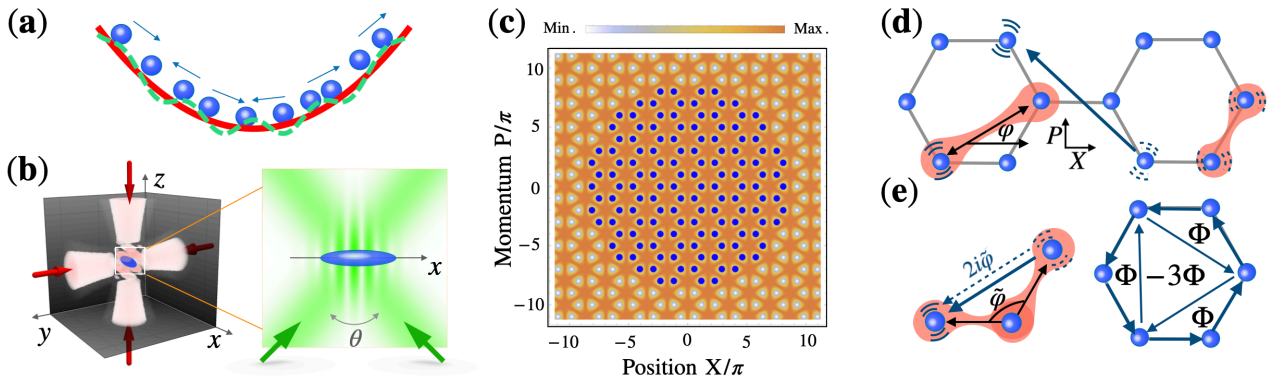


FIG. 1. **(a)** Sketch of our model: particles (blue) confined in a static harmonic potential (red) and driven by stroboscopic lattices (green). **(b)** Experimental implementation of our model with a cloud of cold atoms (blue) confined in quasi-1D tubes by two orthogonally polarized lasers (pink) and subject to a tuneable stroboscopic lattice formed by two lasers (green) intersecting at angle θ. **(c)** Density plot of single-particle Hamiltonian $H_s(X,P)$, with X,P in a rotating frame. The honeycomb lattice sites are occupied by atoms (blue), forming a disk-shaped crystal in phase space. **(d)** Sketch of coupling between the atoms' vibrations. The arrow indicates hopping of a vibrational excitation. The pink dumbbell-like shapes indicate pairwise creation (annihilation) of excitations. **(e)** Sketch of the pairing-interaction-induced hopping (left panel) and the resulting effective magnetic field (right panel). The induced non-reciprocal hopping pathway (dashed arrow) interferes with a direct hopping pathway (solid arrow), leading to a weak staggered magnetic flux of order $\sim\gamma/\omega_0$, see more discussion in Appendix B 3.

chiral transport in phase space. In Sec. VI, we show that the disk-shaped phase space crystal of finite size supports chiral edge states and discuss how to observe the ensuing robust transport in a cold-atom experiment. In Sec. VII, we explore the connection between our phase-space dynamics and an important condensed matter scenario: the 2D real space dynamics of charged particles in an intense magnetic field. In particular, we discuss the implications of our work for the dynamics of the guiding centers of an ensemble of particles frozen in the Lowest-Landau-Level (LLL). In Sec. VIII, we summarise our results and give an overview of possible future research directions.

II. PHASE SPACE LATTICE

A. Honeycomb lattice in phase space

Consider cold atoms trapped in a quasi-1D elongated harmonic potential with the axial trapping frequency ω_{ax} and transverse trapping frequency $\omega_{tr}\gg\omega_{ax}$. The atoms are driven stroboscopically by multiple optical lattices with kicking frequency ω_{ax}/τ, where τ is the dimensionless kicking period. We sketch our model and the experimental implementation in Fig. 1(a)-(b). The single-atom Hamiltonian is given by

$$\tilde{H}_s=\frac{1}{2}(x^2+p^2)+\sum_{n\in\mathbb{Z}}\sum_q K_q\cos(k_q x-\phi_q)\delta\Big(\frac{t}{\tau}-\theta_q-n\Big). \tag{1}$$

Here, we have rescaled the coordinate, momentum, time and energy by k^{-1}, $m\omega_{ax}/k$, ω_{ax}^{-1} and $m\omega_{ax}^2/k^2$, respectively, where m is the mass and k is the typical wave vector of the stroboscopic lattices. This model is a generalization of the well-known kicked harmonic oscillator[25–30] in that it allows for pulses with different wavelengths k_q.

For weak near-resonant driving ($|K_q|\ll 1$, $\tau/2\pi\approx 1$), the single-particle dynamics is dominated by fast harmonic oscillations with slowly changing quadratures (X,P):

$$\begin{cases} x(t)=P\sin\left(\frac{2\pi t}{\tau}\right)+X\cos\left(\frac{2\pi t}{\tau}\right)\\ p(t)=P\cos\left(\frac{2\pi t}{\tau}\right)-X\sin\left(\frac{2\pi t}{\tau}\right).\end{cases} \tag{2}$$

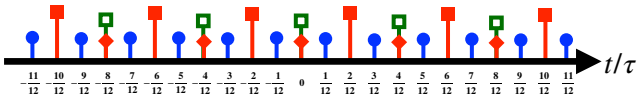
Within rotating-wave approximation (RWA) this leads to a time-independent Hamiltonian (see Appendix A for detailed derivation)

$$H_s(X,P)=\frac{1}{2}\delta\omega\left(P^2+X^2\right)+\sum_q K_q\cos\Big[k_q\Big(P\sin 2\pi\theta_q+X\cos 2\pi\theta_q\Big)-\phi_q\Big], \tag{3}$$

where $\delta\omega\equiv 1-2\pi/\tau$ is the detuning between driving and harmonic frequencies. The extrema of $H_s(X,P)$ represent stable points. In the standard kicked harmonic oscillator[25–30] and for an appropriate choice of the parameters, the stable points can form a square or triangular bravais lattice. Our more general model allows for more flexibility in the design of $H_s(X,P)$ and, in particular, to realize any arbitrary phase-space lattice (see more details in Appendix A).

For concreteness, in the remainder of the paper, we focus on a scenario where $H_s(X,P)$ supports a honeycomb lattice of stable points. By superposing twelve equally spaced kicks as shown in Fig. 2, we have the following

	θ_q	K_q	k_q	ϕ_q
	$\frac{1}{12}, \frac{3}{12}, \frac{5}{12}, \frac{7}{12}, \frac{9}{12}, \frac{11}{12}$	$\frac{1}{2}\Lambda$	2	0
	$\frac{0}{12}, \frac{4}{12}, \frac{8}{12}$	$\frac{1}{2}\Lambda$	$\frac{4}{\sqrt{3}}$	π
	$\frac{2}{12}, \frac{6}{12}, \frac{10}{12}$	Λ	$\frac{2}{\sqrt{3}}$	π
	$\frac{0}{12}, \frac{4}{12}, \frac{8}{12}$	$\frac{2}{\sqrt{3}}\Delta$	$\frac{2}{\sqrt{3}}$	$\frac{3}{2}\pi$



Kicking sequence

FIG. 2. Kicking protocol for the honeycomb lattice: (Top) Kicking parameters table and (Bottom) kicking sequence. The kicks listed in the first three lines lead to the parity-symmetric Honeycom lattice Hamiltonian, i.e., second term in Eq. (4). The kicks in the fourth line induce the parity-symmetry breaking Hamiltonian, i.e., third term in Eq. (4).

single-particle Hamiltonian (up to a constant $3\Lambda/2$),

$$H_s(\boldsymbol{Z}) = \frac{1}{2}\delta\omega|\boldsymbol{Z}|^2 - \frac{16}{9}\omega_0 \prod_{n=1}^{3} \sin^2\left(\frac{1}{2}\boldsymbol{v}_n \cdot \boldsymbol{Z}\right) - \frac{2\Delta}{\sqrt{3}} \sum_{n=1}^{3} \sin\left(\boldsymbol{v}_n \cdot \boldsymbol{Z}\right). \quad (4)$$

Here, we have defined the vector $\boldsymbol{Z} \equiv (X, P)$, and three ancillary vectors $\boldsymbol{v}_1 = (\frac{2\sqrt{3}}{3}, 0)$, $\boldsymbol{v}_2 = (-\frac{\sqrt{3}}{3}, 1)$, $\boldsymbol{v}_3 = (-\frac{\sqrt{3}}{3}, -1)$. For $\delta\omega = 0$, the minima of $H_s(\boldsymbol{Z})$ form a honeycomb lattice, cf. Fig. 1(c). The frequency of small vibrations about these stable points $\omega_0 = -9\Lambda$ can be obtained by the linear expansion of Eq. (4). The last term in the Hamiltonian (4) breaks the inversion symmetry of the honeycomb lattice and, thus, allows for different onsite energies of the two sublattices $\omega_L = \omega_0 \pm 2\Delta$. We note that $[X, P] = i\lambda$ with the effective Planck constant $\lambda = \hbar k^2/m\omega_{ax}$, which is twice the square of the Lamb-Dicke parameter[31]. The condition $\lambda \ll 1$ ensures that the quantum fluctuations are small compared to the phase-space distance between neighboring stable points. In the reminder of this paper, we will focus on this parameter regime.

B. Symmetries in phase space

Next, we analyze how the time and space symmetries of the full lab-frame Hamiltonian Eq. (1) are reflected into the phase-space symmetries of the RWA Hamiltonian Eq. (3). For concreteness, we focus on the special case of our honeycomb lattice Hamiltonian Eq. (4). For the train of pulses displayed in the parameter table in Fig. 2, the full Hamiltonian Eq. (1) has period $\tau/3$, $\tilde{H}_s(t+\tau/3) = \tilde{H}_s(t)$. This is one-third of the rotation period τ of the frame of reference Eq. (2) in which the RWA Hamiltonian is defined. This discrete time-translational symmetry leads to a three-fold rotational symmetry of the Hamiltonian Eq. (4) in phase space.

In addition, the Hamiltonian Eq. (1) has time-reversal symmetry $\tilde{H}_s(-t) = \tilde{H}_s(t)$, cf. the kicking sequence displayed below the parameter table in Fig. 2. The time-reversal symmetry leads to a mirror-symmetry in phase space $H_s(X, -P) = H_s(X, P)$. Because of the tree-fold rotational symmetry, the Hamiltonian $H_s(X, P)$ has actually three different mirror planes. Each such plane corresponds to two difference reference time for the time-reversal symmetry $\tilde{H}_s(-t + n\tau/3) = \tilde{H}_s(t + n\tau/3)$, and $\tilde{H}_s(-t+n\tau/3+\tau/2) = \tilde{H}_s(t+n\tau/3+\tau/2)$, with $n = 0, 1, 2$ for the three different planes.

For the special case where the pulses in the last row of the table in Fig. 2 have zero amplitude (corresponding to $\Delta = 0$), the Hamiltonian Eq. (1) has also parity symmetry $\tilde{H}_s(x) = \tilde{H}_s(-x)$. The parity symmetry leads to an additional mirror plane in phase space, $H_s(-X, P) = H_s(X, P)$. Combined with the time-reversal symmetry $H_s(X, -P) = H_s(X, P)$, it leads to the two-fold rotational symmetry, $H_s(-X, -P) = H_s(X, P)$. Thus, our phase space crystal (for $\Delta = 0$) has the full point-group symmetry $\mathcal{C}_{6\nu}$ (six-fold rotations and six mirror planes) of the underlying triangular Bravais lattice.

III. PHASE SPACE CRYSTAL

A. Phase space interaction

The interaction of neutral cold atoms in a tight 1D-trap is captured by an effective two-body contact potential[32], $V(x_i - x_j) = \gamma\delta(x_i - x_j)$. Since atoms that are localized about distant phase-space points will still collide in the course of their lab-frame trajectories, the lab-frame contact interaction gives rise to an effective long-range interaction in the rotating frame[15,33–36]. For $\lambda \ll 1$, the interaction is Coloumb-like[15,35], $U(\boldsymbol{Z}_i - \boldsymbol{Z}_j) = \gamma\pi^{-1}|\boldsymbol{Z}_i - \boldsymbol{Z}_j|^{-1}$. Thus, we arrive at the many-body Hamiltonian

$$H = \sum_i H_s(\boldsymbol{Z}_i) + \frac{\gamma}{\pi} \sum_{i<j} \frac{1}{|\boldsymbol{Z}_i - \boldsymbol{Z}_j|}. \quad (5)$$

By introducing the *phase space force* $\boldsymbol{F}_i \equiv -\nabla_i H$ with $\nabla_i \equiv (\partial/\partial X_i, \partial/\partial P_i)$ and the unit direction vector $\hat{\boldsymbol{n}}$ perpendicular to the phase space plane, we can rewrite Hamilton's canonical equations as

$$\frac{d}{dt}\boldsymbol{Z}_i = \hat{\boldsymbol{n}} \times \boldsymbol{F}_i. \quad (6)$$

As a result, the phase space force causes a displacement of the atoms perpendicular to the force direction in phase space, which is similar to the Lorentz force.

In the presence of dissipation, the stable points become attractors[37]. In other words, a non-interacting atom

tends to relax towards the closest stable point. Introducing a sufficiently strong repulsive interaction ($\gamma > 0$) and initially preparing the atoms close to the origin will, thus, give rise to a disk-shaped crystal, see Fig. 1(c).

It is important to keep in mind that in a finite geometry the atom-atom interactions tend to distort the equilibrium configuration. We now want to discuss how to mitigate this undesired effect. In a mean-field approximation, the effective electrostatic potential experienced by an atom at phase-space position $\mathbf{Z}_i$ (induced by the remaining atoms) can be approximated by the Coulomb potential for a uniformly charged disk

$$\overline{U}(\boldsymbol{Z}_i) = 2\pi\sigma R\Big[1 - \sum_{l=0}(2l+1)\Big[\frac{(2l-1)!!}{(2l+2)!!}\Big]^2\Big(\frac{|\boldsymbol{Z}_i|}{R}\Big)^{2l+2}\Big]. \tag{7}$$

Here, $\sigma = \gamma/\sqrt{3}\pi^3$ is the effective charge density and we have assumed that the disk of radius R is centered about the origin of phase space. We note that the leading order term ($l = 0$) in the above effective potential represents a harmonic potential $\overline{U}(\boldsymbol{Z}_i) \sim -\sigma\pi R^{-1}|\boldsymbol{Z}_i|^2/2$. We can further improve the fitting of $\overline{U}(\boldsymbol{Z}_i)$ to a parabolic potential (and, thus, partially taking into account the high-order l-th terms) by adjusting the curvature

$$\overline{U}(|\boldsymbol{Z}_i|) \sim -1.35\frac{\sigma\pi}{2R}|\boldsymbol{Z}_i|^2.$$

This effective parabolic potential can be easily counterbalanced by a laser-generated potential, thereby, strongly reducing the lattice distortion. In practice, this can be achieved simply by choosing the appropriate detuning $\delta\omega = 1.35\sigma\pi R^{-1}|\boldsymbol{Z}|^2/2$ in Hamiltonian (4) instead of resonant driving, cf. Fig. 5(a).

B. Dynamics of crystal vibrations

Each atom oscillates around its equilibrium position, i.e., $\boldsymbol{Z}_L(t) = \boldsymbol{Z}_L^0 + \boldsymbol{u}_L(t)$ where $\boldsymbol{u}_L = (u_L^X, u_L^P)$ is the displacement on the lattice site L. The equilibrium points are determined by $\partial H/\partial u_L^\alpha = 0$ ($\alpha \in \{X, P\}$). By expanding the Hamiltonian Eq. (5) up to second order, we rewrite it in terms of the classical variable $\alpha_L \equiv \frac{1}{\sqrt{2\lambda}}(u_L^X + iu_L^P)$ (see detailed derivation in Appendix B 2)

$$\mathcal{H} = \sum_L \omega_L\alpha_L^*\alpha_L + \frac{1}{2}g_L\alpha_L^{*2} + \frac{1}{2}g_L^*\alpha_L^2 - \frac{\gamma}{4\pi}\sum_{L\neq L'}\frac{\alpha_L^*\alpha_{L'} + 3e^{i2\varphi_{LL'}}\alpha_L^*\alpha_{L'}^*}{|\boldsymbol{Z}_L^0 - \boldsymbol{Z}_{L'}^0|^3} + h.c. \tag{8}$$

Here ω_L are the onsite quasienergies with $\omega_L - \omega_0 \sim \mathcal{O}(\gamma)$, and $\varphi_{LL'}$ is the angular coordinate of $\boldsymbol{Z}_L^0 - \boldsymbol{Z}_{L'}^0$, cf. Fig. 1(d), defined via

$$\begin{cases} X_L - X_{L'} = R_{LL'}\cos\varphi_{LL'}, \\ P_L - P_{L'} = R_{LL'}\sin\varphi_{LL'}. \end{cases} \tag{9}$$

The Hamiltonian Eq. (8) describes phonons propagating in our honeycomb phase-space crystal. It is reminiscent of the tight-binding model for electrons in graphene, but with two qualitatively new features: (i) Our phase-space phonons can hop between any two arbitrarily distant sites reflecting the long-range nature of the atom-atom interaction, as indicated by the blue arrow in Fig. 1(d); (ii) The excitation-number is not conserved, because a phonon pair can be created or annihilated on any pair of sites.

It is important to highlight an important qualitative feature of our model for the phase-space vibrations: *the complex phases $\varphi_{LL'}$ of the anomalous pairing interaction have a geometrical interpretation as the angular coordinate of the link connecting two sites,* cf. Eq. (9) and Fig. 1(d). The same interpretation will still hold for any arbitrary phase-space single-particle Hamiltonian $H_s(\boldsymbol{Z})$ and atom-atom interaction $U(\boldsymbol{Z}_i - \boldsymbol{Z}_j)$ (see Appendix B 2 for a more detailed discussion) and, thus, is to be viewed as a general property of vibrations in phase space. This is in stark contrast to the non-reciprocal phases of tight-binding Hamiltonians in 2D real space which can be tuned without displacing the lattice sites. Below, we show that this complex phases lead to a topological phase transition.

IV. TOPOLOGICAL BAND STRUCTURE

A. Connection to QAHE

In order to better distinguish the effects of the (long-range) hopping and the pairing interaction, it is instructive to first consider a regime where the latter is suppressed. This will be the case if the creation of phonon pairs is far off-resonant, for $\gamma \ll \omega_0$. The band structure in this regime is shown in Fig. 3(a). While the long-range hopping strongly modifies it compared to its graphene counterpart, its main distinguishing feature is still on display: it supports two Dirac cones at the high-symmetry points K and K', with the tips of the cones separated by a small gap. We note that the Dirac cones are symmetry-protected (they should be gapless if the Hamiltonian has six-fold rotational symmetry and real hopping amplitudes). Thus, the small band gap must be induced by the complex amplitudes of the pairing perturbation. In 2D real space, the appearence of such complex amplitudes would be interpreted as being induced by the breaking of the time-reversal symmetry and is well known to lead to a topological band gap[3].

This can be further substantiated by observing that, in the off-resonant regime, the main effect of the pairing interaction is to induce effective hopping transitions with non-reciprocal phases, cf. left subfigure in Fig. 1(e). Thus, a phonon propagating on a close loop $L(\cdot)$ will acquire a geometrical Berry phase $\Phi(L(\cdot))$. These geometrical phases are similar to the Aharonov-Bohm phases acquired by charged particles in a magnetic field and are,

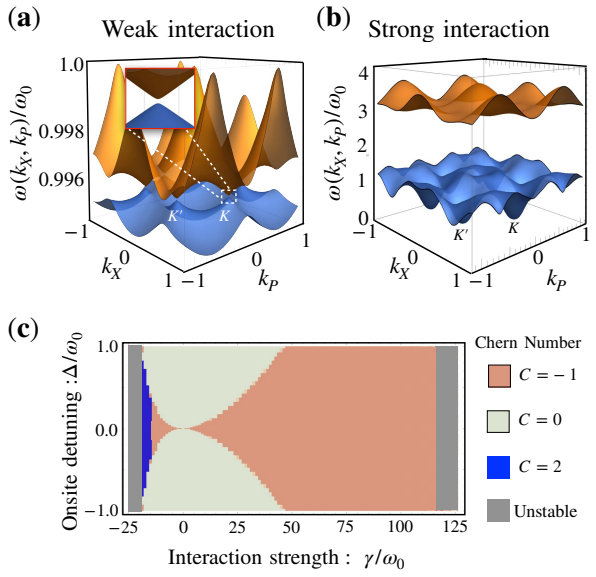


FIG. 3. Bulk band structures for weak interaction strength $\gamma/\omega_0 = -0.2$ **(a)** and strong interaction $\gamma/\omega_0 = 102$ **(b)**. Topological phase diagram **(c)** with Chern number C (the Chern number of the lowest band) as a function of interaction strength γ and on-site detuning Δ, which lifts the degeneracy at the K (K') symmetry points.

thus, often referred to as synthetic magnetic fluxes. In fact, we can derive an effective particle-conserving description from a perturbation theory in γ/ω_0. That is to say, the pairing term $\propto \alpha_L^* \alpha_{L'}^*$ in the Hamiltonian (8) can be cancelled and replaced by a hopping term $\tilde{h}_{LL'}\alpha_L^*\alpha_{L'}$ with pairing-induced hopping rate given by (see the detailed derivation in Appendix B 3)

$$\tilde{h}_{LL'} \approx -\Big(\frac{3\gamma}{2\pi}\Big)^2 \sum_{\bar{L}} \frac{2}{\omega_{\bar{L}}} \frac{1}{R_{L\bar{L}}^6} e^{i2(\varphi_{L\bar{L}} - \varphi_{L'\bar{L}})}. \quad (10)$$

In Fig. 1(e), we show the geometric angle $\tilde{\varphi} \equiv \varphi_{L\bar{L}} - \varphi_{L'\bar{L}}$ and the resultant phase exponent $2i\tilde{\varphi}$ of complex pairing-induced hopping rate. This differs from the well-known Haldane model for the anomalous Quantum Hall effect[3] only in that it includes long-range hopping transitions. As for the Haldane model, the non-reciprocal hopping phases can be viewed as being induced by an effective staggered magnetic field, cf. right subfigure in Fig.1(e), and open a small topological gap of width $\sim \gamma^2/\omega_0$ and with band-gap Chern number $C = -1$, cf. Fig. 3(a). We emphasize that this synthetic *staggered* magnetic field for phonons is a purely *classical* effect and is not to be confused with the *uniform* synthetic magnetic field that can be introduced to describe the motion of a single *quantum* atom in a non-commutative phase space[13–18].

B. Strong interaction regime

In the strong interaction regime, $|\gamma| \gg |\omega_0|$, the phonon number is not even approximately conserved due to the pairing interactions in Hamiltonian (8) and it is, thus, not possible to employ a single-particle description. The physics is also different compared to superconducting systems[38] (with fermionic pairing-interactions): for bosons, there is no limit to the occupation number of single-particle states, which can lead to the amplification of fluctuations and even to instabilities[8,39,40].

In the stable regime, the Hamiltonian (8) can be diagonalized via a bosonic Bogoliubov transformation (see Appendix C). For the bulk, $\mathcal{H} = \sum_{\boldsymbol{k},n=1,2} \omega_{\boldsymbol{k},n} |\beta_{\boldsymbol{k},n}|^2$ where $\boldsymbol{k} = (k_X, k_P)$ is the quasi-momentum, $\omega_{\boldsymbol{k},n}$ is the band structure, and $\beta_{\boldsymbol{k},n}$ are the normal modes,

$$\beta_{\boldsymbol{k},n}^* = \sum_{s=A,B} u_{n,s}(\boldsymbol{k}) \alpha_{\boldsymbol{k},s}^* + v_{n,s}(\boldsymbol{k}) \alpha_{-\boldsymbol{k},s}$$

with $\alpha_{\boldsymbol{k},s} \equiv \frac{1}{\sqrt{N}} \sum_l \alpha_{l,s} e^{-i\boldsymbol{k}\cdot\boldsymbol{Z}_{l,s}^0}$ (N is the number of primitive cells). The band Chern number is defined by (see Appendix C 2)

$$C = \frac{1}{2\pi} \int_{BZ} \big(\nabla_k \times \mathcal{A}_1(\boldsymbol{k})\big) \cdot \hat{z} \quad (11)$$

where

$$\mathcal{A}(\boldsymbol{k}) = i \sum_s [u_{1,s}^*(\mathbf{k}) \nabla_{\boldsymbol{k}} u_{1,s}(\mathbf{k}) - v_{1,s}^*(\mathbf{k}) \nabla_{\boldsymbol{k}} v_{1,s}(\mathbf{k})] \quad (12)$$

is the Berry connection for the lower band. Note that the definition of the Berry connection Eq. (12) has to be modified compared to the standard definition to account for the Bosonic nature of our excitations[8]. In a classical setting, the Chern number quantization as well as the other usual properties of the Chern number (including the bulk-boundary correspondence[41]) follow from the conservation of the Poisson brackets $\{\beta_{\boldsymbol{k}',n'}^*, \beta_{\boldsymbol{k},n}\} = i\delta_{n,n'}\delta_{\boldsymbol{k}',\boldsymbol{k}}$ (or, equivalently, $\sum_s |u_{n,s}|^2 - |v_{n,s}|^2 = 1$).

The band structure for a comparatively strong interaction is shown in Fig. 3(b). In this case, the Chern number $C = -1$ remains the same as in the weak-interaction limit. We note that close to the K and K'-points (as labelled in the figure) the lowest band approaches zero quasienergy. In the presence of bosonic pairing interactions, the quasienergy can be viewed as the energy cost of producing a pair of Bogoliubov excitations. When this hits zero for a critical threshold $\gamma_c^+ \approx 115\omega_0$ or $\gamma_c^- \approx -20\omega_0$, the phase space crystal becomes unstable, leading to a disordered gas phase.

C. Topological phase diagram

We have systematically investigated our phase space crystal by varying the interaction strength but also allowing for different onsite quasienergies, $\omega_L \equiv \omega_0 \pm 2\Delta$, for the two honeycomb sublattices, cf. Eq. (4). The onsite detuning Δ, which is engineered using additional stroboscopic lasers, breaks the inversion symmetry, allowing

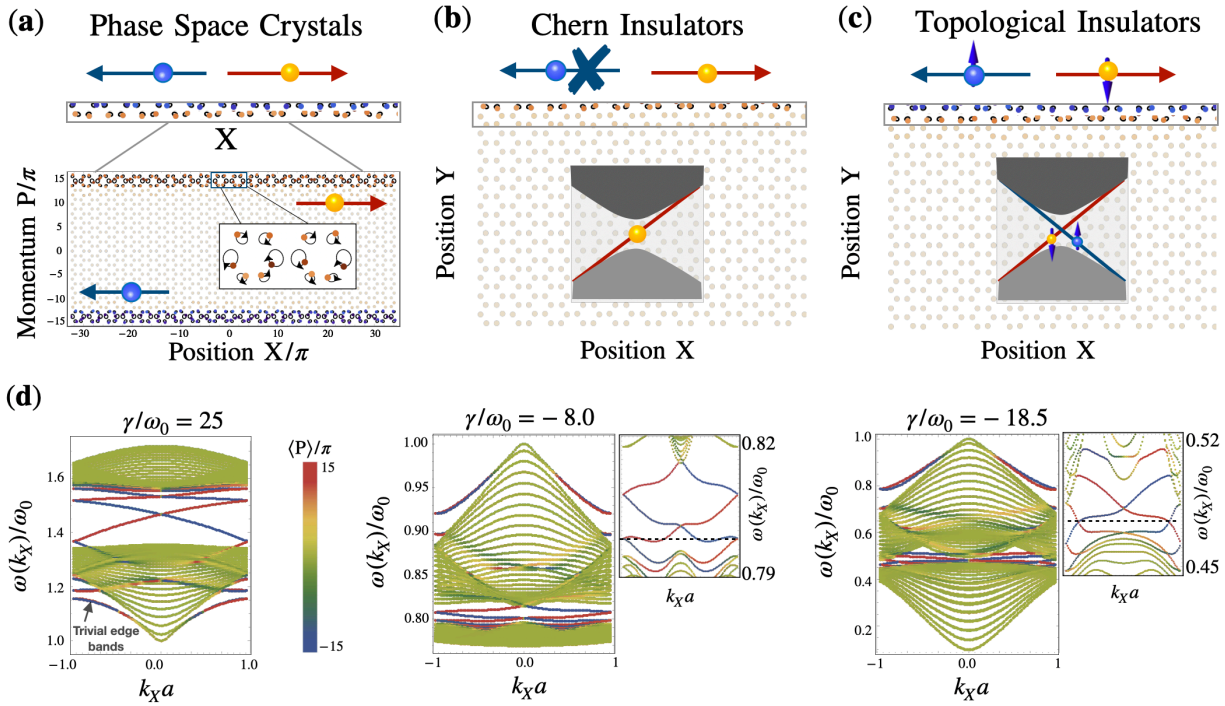


FIG. 4. **Topological edge states.** **(a)** Strip-shaped phase-space crystal with two topological edge states propagating on the boundaries. Inset shows atoms' orbits (circles) and vibration energy (colour). Upper figure represents 1D system in real space. **(b)-(c)** Topological transport on the edge of 2D real-space Chern insulators (b), time-reversal symmetric topological insulators (c). The two inserts indicate typical topological band structures of the strip for each case. **(d)** Band structures of the strip-shaped phase space crystal for interaction strengths $\gamma/\omega_0 = 25$ (left), $\gamma/\omega_0 = -8.0$ (middle) and $\gamma/\omega_0 = -18.5$ (right). The colour indicates the average P of each eigenstate, the insets in the middle and right figures are the zoomed-in band structures around the energy gap and $a = 4\pi/\sqrt{3}$ is the lattice constant in X direction of the strip. For 2D real-space Chern insulators (b), the edge states do not have a time-reversed partner leading to *chiral* transport. For time-reversal symmetric topological insulators (c), each edge state has a time-symmetric partner co-localized on the same boundary but with opposite spin (or out-of-plane mirror symmetry) and propagation direction. This leads to *helical* transport. Also for our phase-space crystal (a), an edge state have a time-reversed partner (in the ideal case of two open separated boundaries). However, the two edge states (without any internal degree of freedom) have the same chirality and are not co-localized in phase space.

a trivial band gap. The ensuing topological phase diagram is shown in Fig. 3(c). For $\Delta = 0$, the phase-space crystal has Chern number $C = -1$ for a broad range of attractive and repulsive interactions, but can also switch to $C = 2$ for negative interactions, before becoming unstable. The $C = 2$ topological phase is not present in the Haldane model[3]. In the region of weak interactions, the band edge is cone-shaped and the band gap scales as γ^2/ω_0 for $\Delta = 0$. In this regime, the gap determines how far the topological region extends into the $\Delta \neq 0$ region.

V. TOPOLOGICAL BOUNDARY STATES AND TIME-REVERSAL SYMMETRY

In two-dimensional *real* space, the time-reversal transformation changes the chirality of trajectories, e.g., from clockwise to anti-clockwise. For this reason, robust chiral edge states – without a time-reversed partner with opposite chirality – can be implemented in 2D real space only after breaking the TRS. However, this constraint does not apply to phase-space crystals, because the chirality of motion in phase space remains unchanged under a time-reversal transformation. Indeed, because of the complex phases $\varphi_{LL'}$, Hamiltonian (8) does not support any local anti-unitary symmetry. This is, in fact, the standard formal precondition for non-trivial Chern numbers and chiral edge states[42,43]. For phase-space crystals, it can be fulfilled even though the time-reversal remains a symmetry, because this symmetry rearranges the phase-space crystal in a non-local fashion, i.e., $(X_i, P_i) \to (X_i, -P_i)$ for all the atoms.

It is interesting to investigate how this unusual status of the time-reversal symmetry bears on the topological edge states of a phase space crystal. For concreteness, we initially focus on the conceptually simple scenario of a strip. For simplicity we neglect the small deformations of the lattice equilibrium configurations induced by the atom-atom interactions.

In Fig. 4(a), we display two edge states for vibrations about an equilibrium configuration that is invariant under time-reversal symmetry (the amplitude of the vibra-

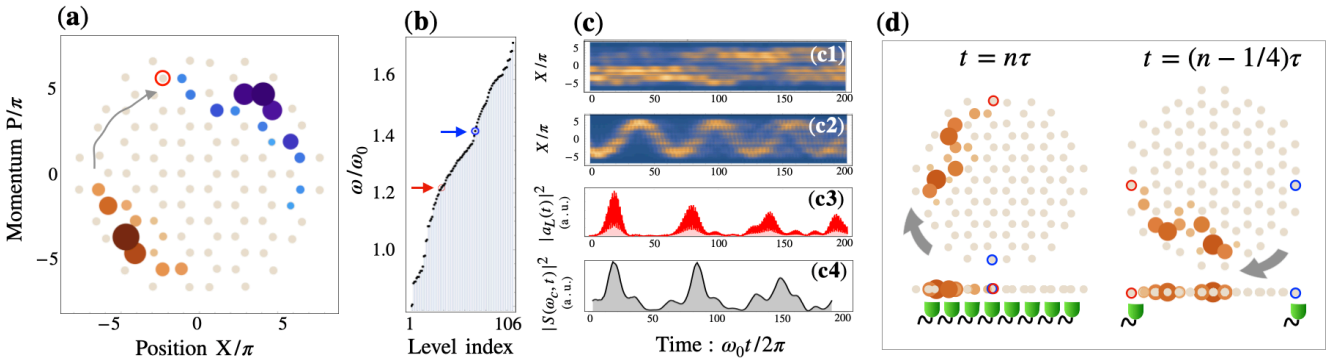


FIG. 5. **Chiral transport on the edge of disk-shaped phase-space crystal.** **(a)** One edge channel wave packet at different temporal instants. **(b)** Energy spectrum with arrows indicating the energy level centres for constructing the wave packet in (a) by the Gaussian superposition of eigenstates around them. **(c1)-(c2)** Spacetime plot of wave packet projected on the spatial X dimension. The central frequencies ω_c of wave packets in (c1) and (c2) are indicated by the red and blue arrows in (d) respectively. **(c3)** Vibration $|a_L(t)|^2$ of the atom marked by red circle in (a). **(c4)** Finite-time-window power spectrum $S(\omega_c, t)$ of a collective signal from all the atoms. **(d)** Detection of chiral direction. (Left) At stroboscopic time steps $t = n\tau$ with $n \in \mathbb{Z}$, an array of detectors are placed along the 1D system in real space to measure the distribution of vibrations over the 1D real space. (Right) At earlier time moments $t = (n - 1/4)\tau$, the atoms (marked with red and blue circles) that are close in real space at stroboscopic time moment become separated at the two ends of 1D system in real space and thus can be detected independently. [Parameters: interaction $\gamma = 25\omega_0$ for all figures; disk radius $R = 8\pi$ and $\delta\omega = 1.35\sigma\pi R^{-1}$; time window $\Delta t = 10 \times 2\pi\omega_0^{-1}$ for (c4)]

tions is encoded using two different color scales to distinguish the two different states). In addition, we show the band structure for three different values of the system parameters in the topological phases $C = -1$ and $C = 2$, cf. Fig. 4(d). We note that for any energy inside the band gap the net number of topological edge states (difference between anti-clokwise movers and clockwise movers) on each of the boundaries is equal to the band gap Chern number as predicted by the bulk-boundary correspondence[20]. According to this correspondence, the edge states on opposite phase-space boundaries have the same chirality and, thus, opposite propagation directions, cf. Fig. 4(a).

For the special case considered here, where the time-reversal is a symmetry, the edge states on the two boundaries are obtained one from the other by applying the time-reversal transformation. We note that the two states are co-localized in real space, cf. upper figure in Fig. 4(a). In spite of this, their coupling is exponentially suppressed with the phase space separation (in this geometry the width of the strip), leading to topologically robust transport. This is in stark contrast to time-reversal symmetric topological insulators[44,45] whose time-reversal partner edge states have opposite chirality, do not have any spatial separation and remain decoupled only as long as the time-reversal symmetry is not broken by the disorder, cf. Fig. 4(c). Our situation is also different compared to standard Chern insulators which do not support any time-reversed partner solution, cf. Fig. 4(b). This conclusion holds true also for Chern insulators of systems with one real and one synthetic dimension[21,22]: these systems will support counter-propagating edge states that are co-localized in the single real dimension but are NOT time-reversal partners.

VI. TOPOLOGICAL TRANSPORT

We now turn to a realistic disk-shaped crystal with a randomly-shaped boundary [Fig. 5(a)]. Here, we fully take into account the atom-atom interaction that deforms the equilibrium configuration. As discussed above, one can reduce the deformation using a finite laser detuning $\delta\omega = 1.35\sigma\pi R^{-1}|\boldsymbol{Z}|^2/2$ in Eq. (4), cf. discussion about Eq. (7). In Fig. 5(a), we illustrate the chiral transport by tracking the time evolution of a wave packet with average quasienergy ω_c in the middle of the band gap, cf. blue arrow in Fig. 5(b). It can be readily observed that the transport is robust against the boundary defects[46]. In Figs. 5(c1)-(c2), we compare the non-chiral and chiral transports by projecting the evolution of the wave packet onto the coordinate X in the rotating frame. The time evolution of a single atom's vibrational energy likewise reveals the periodicity of the packet traversing the disk's circumference, cf. Fig. 5(c3). However, in any real experiment, it might be easier to obtain a collective signal from all the atoms, for example by light scattering: $I(t) = \sum_j \cos[k_s X_j(t)]$ obtained by using a stroboscopic optical lattice for detection. One can extract the finite-time-window power spectrum

$$S(\omega, t) \propto \left| \left\langle (I(t) - \langle I \rangle) e^{i\omega t} \right\rangle_{\Delta t} \right|^2,$$

where $\langle \cdots \rangle_{\Delta t}$ represents the time average over a finite time window. In Fig. 5(c4), we plot the power spectrum $S(\omega_c, t)$ (at $k_s = 9.95$) as a function of time. The periodic

temporal peaks of S nicely indicate the chiral motion of the wave packet.

The parameters used for Figs. 5(a)-(c) could be obtained in an experiment with ultracold ^{87}Rb atoms. An appropriate experimental setup involves 8 lasers (4 for the static trapping, 2 for the stroboscopic trapping and 2 for the optomechanical detection), see sketch by Fig. 1(a). Assuming a realistic longitudinal trapping frequency $\omega_{ax} = 2\pi \times 50\,\mathrm{Hz}$ and $\omega_0 = 0.1$ (to guarantee slow vibrations in the rotating frame), the wavepacket's time of flight during a round-trip along the disk edge would be approximately $2\pi \times 50/(\omega_{ax}\omega_0) \approx 10\,\mathrm{s}$, shorter than the typical lifetime of the atom cloud[47–49]. With $k^{-1} = 45\,\mu\mathrm{m}$, one works in the semi-classical regime ($\lambda = 0.04$). In the experiment, the transverse trapping frequency can reach up to $\omega_{tr} \approx 2\pi \times 1.0\,\mathrm{MHz}$[32]. To avoid exciting the transverse mode during collisions, there is a restriction for the radius of the phase space crystal, $R < k\sqrt{\frac{\hbar\omega_{tr}}{m\omega_{ax}^2}} \approx 9.2\pi$, cf. Appendix D 4. Taking into account the 3D scattering length $a = 5.3\,\mathrm{nm}$ for ^{87}Rb atoms, the 1D dimensionless interaction strength is $\gamma = 2\hbar\omega_{tr}ak^3/(m\omega_{ax}^2) \approx 1.25$, which can be further tuned by Feshbach resonance, cf. Appendix D 3, or adjusting k.

A. Detection of chiral direction

Measurement traces as in Figs. 5 (c2) (time trace of a quadrature) or (c3) (vibrational amplitude of a single-atom) would demonstrate the existence of robust chiral motion. However, they do not yet allow to detect its chirality (clockwise or anti-clockwise). To infer the time trace of a quadrature as displayed in Figs. 5(c2), one could measure the local vibrations, as in Figs. 5(c3), by placing detectors at the atom cloud, as illustrated by Fig. 5(d). This seems to lead to an ambiguity: since the disk-shaped cloud is actually one-dimensional in real space it seems that any local measurement could not distinguish between atoms that are close in real space but have different momentum, e.g., the two atoms marked by the red and blue circles in the left panel of Fig. 5(d). Without the ability to distinguish these opposite phase-space configuration, it is also not possible to determine the direction of the chiral motion. However, it is important to keep in mind that the fixed equilibrium position of the atoms in the rotating frame should be viewed as the result of taking a series of snapshots of the atom cloud at the stroboscopic time steps $t = n\tau$ with $n \in \mathbb{Z}$ and τ being the stroboscopic time step. On the other hand, in the lab-frame continuous time picture, the whole phase space crystal structure rotates clockwise in phase space as indicated by the arrows in Fig. 5(d). Importantly, the same experimental setup allows to monitor the motion for different stroboscopic time series, e.g. with a one quarter of harmonic period earlier $t = (n - 1/4)\tau$, $n \in \mathbb{Z}$. The resulting measurement trace allows to distinguish the atoms marked by the red and blue circles. Thus, by comparing the two traces taken with a different stroboscopic time series, one could deduce the chiral direction from the delay between the vibrational peaks. This is even possible if the motion is only monitored close to the boundaries of the cloud (which should be experimentally easier), cf. the right panel of Fig. 5(d).

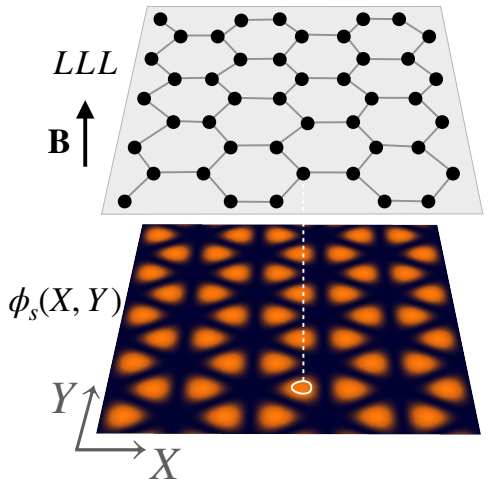


FIG. 6. Real-space implementation for ions or semiconductor electrons - vibrations of cyclotron guiding centres in a strong magnetic field $\boldsymbol{B}$. Cyclotron orbital centres (upper panel) in LLL subjected to an external honeycomb lattice potential $\phi_s(X, Y)$ (lower panel).

VII. IMPLICATIONS FOR REAL SPACE MOTION

The phase-space dynamics investigated here could also be realized in 2D real space using ions in a magnetic field. In an out-of-plane magnetic field $\boldsymbol{B} = B\hat{\boldsymbol{n}}$, the motion of the ions can be decomposed into the cyclotron motion and the drift of the cyclotron guiding center. The two guiding center coordinates $\mathbf{Z} = (X, Y)$ constitute an effective phase space due to $[X, Y] = -i\hbar/qB$ in quantum mechanics[50]. If all the relevant energy scales are much smaller than the cyclotron energy $\hbar\omega_c = \hbar|q|B/m$, the motion is frozen into the lowest Landau level (LLL). The classical dynamics of the guiding center is governed by

$$\frac{d}{dt}\mathbf{Z}_i = (qB)^{-1}\boldsymbol{F}_i \times \hat{\boldsymbol{n}}, \tag{13}$$

similar to the phase-space dynamics given by Eq. (6). Considering that the phase-space interaction Eq. (5) has the Coulomb form, our model is implemented in the 2D external electrostatic potential $\phi_s(\boldsymbol{Z}) \propto H_s(\boldsymbol{Z})$, cf. Eq. (4). We illustrate the real-space implementation for ions or semi-conductor electrons in Fig. 6.

We note that for filling factors $\nu \equiv 2\pi n\hbar/eB$ (where n is the density) below a critical threshold $\nu_w \sim \frac{1}{7}$,

the ground state of the ions is expected to be a crystal even without any external confining potential[51,52], a so-called Wigner Crystal[53,54]. However, in this case the guiding centers are known to be arranged on a simple Bravais triangular lattice, leading to a single trivial phonon band[54–56]. Our work shows that when the guiding centers are rearranged on a honeycomb lattice by an external electrostatic potential $\phi_s(X,Y)$, the crystal vibrations become topological. In this context, it is instructive to revisit our results in Fig. 3. The presence of topological phases with different sign of the Chern number C indicates that the chirality of the vibrations can be reversed. Counterintuitively, for $C=2$ corresponding to strong repulsive interactions γ, the chirality of the phonon edge states is opposite compared to the chirality of the cyclotron orbits, cf. Fig. 5(d).

VIII. SUMMARY AND OUTLOOK

In summary, we have investigated the vibrational modes of phase space crystals formed by atoms that are periodically arranged in phase space. We provided a general method for generating arbitrary lattice structures in phase space. We have shown that the small vibrations of this type of crystal structures can display gapless topologically robust chiral motion, even when the time-reversal is a symmetry. These topological phases are encoded in the symplectic Chern numbers of the bulk bands. Formally, the non-zero Chern numbers are induced by complex amplitudes of the two-mode pairing interactions. Interestingly, the complex phases of these amplitudes have a geometrical interpretation as the angular coordinate of the line connecting two atoms and can not be eliminated by a transformation that is local in phase-space. In addition, we have presented a realistic implementation of our phase crystal and also discussed a scheme to detect the chiral vibrations. Finally, we explored the non-trivial implication of our investigation for the classical motion of charged particles in 2D real space under a strong magnetic field and an additional electrostatic potential.

There are several possible research directions in the future beyond the present work. Robust topology produced by the combination of symplectic phase-space geometry and interactions represents a versatile concept that can be implemented in many physical platforms. For atoms with spin, one would obtain nonlocal spin-dependent interactions in phase space[15,57], coupling spin waves to topological phase-space phonons. Long-range real-space interactions permit the exploration of higher-dimensional generalizations of the physics discussed here in 1D. More complex driving can be used to synthesize arbitrary phase-space potentials[58], and single-shot measurements of multi-atom configurations will allow the observation of additional effects like nonlinear evolution.

ACKNOWLEDGMENTS

We acknowledge helpful discussions with Tirth Shah, Panagiotis Kotetes and Herrmann Schulz-Baldes.

Appendix A: Arbitrary Phase Space Lattice

1. General form

We discuss how to synthesize arbitrary lattice structures in phase space via multiple stroboscopic lattices. We start from the following generalised model of kicked harmonic oscillator

$$H_s=\frac{1}{2}(x^2+p^2)+\sum_{n\in\mathbb{Z}}\sum_q K_q\cos(k_q x-\phi_q)\delta\Big(\frac{t}{\tau}-\theta_q-n\Big). \tag{A1}$$

Here q represents the kicking sequence of stroboscopic lattices whose intensity K_q, wave vector k_q and phase ϕ_q can be tuned at different time instances $t=\tau(n+\theta_q)$ with $n\in\mathbb{Z}$. To simplify the discussion, we first consider a single kick,

$$H_s=\frac{1}{2}(x^2+p^2)+K_q\cos(k_q x-\phi_q)\delta\Big(\frac{t}{\tau}-\theta_q-n\Big). \tag{A2}$$

We transform the above Hamiltonian into rotating frame with kicking frequency $2\pi/\tau$ using the generating function of the second kind

$$G_2(x,P,t)=\frac{xP}{\cos(2\pi t/\tau)}-\frac{1}{2}x^2\tan\big(\frac{2\pi}{\tau}t\big)-\frac{1}{2}P^2\tan\big(\frac{2\pi}{\tau}t\big). \tag{A3}$$

The corresponding canonical transformation is given by

$$p=\frac{\partial G_2}{\partial x},\quad X=\frac{\partial G_2}{\partial P},$$

which results in the transformation of phase-space coordinates

$$\begin{cases} x=P\sin\left(\frac{2\pi t}{\tau}\right)+X\cos\left(\frac{2\pi t}{\tau}\right)\\ p=P\cos\left(\frac{2\pi t}{\tau}\right)-X\sin\left(\frac{2\pi t}{\tau}\right).\end{cases} \tag{A4}$$

and the transformed Hamiltonian

$$H_s(X,P,t)=H_s(x,p,t)+\frac{\partial G_2}{\partial t}=\frac{1}{2}\delta\omega(X^2+P^2)+$$
$$K_q\cos\Big[k_q\big(P\sin\frac{2\pi t}{\tau}+X\cos\frac{2\pi t}{\tau}\big)-\phi_q\Big]\delta\Big(\frac{t}{\tau}-\theta_q-n\Big). \tag{A5}$$

Here, we have defined the global detuning parameter $\delta\omega\equiv 1-2\pi/\tau$ between kicking and harmonic oscillation. For weak resonant driving ($|K_q|\ll 1$, $\delta\omega=0$), the single-particle dynamics can be separated by the fast harmonic oscillation and the low motion of its quadratures (X,P). The effective slow dynamics of quadratures (X,P) is given by the lowest-order Magnus expansion,

i.e., the time average of $H_s(X,P,t)$ in one kicking time period,

$$H_s(X,P) = \frac{1}{\tau}\int_0^\tau H_s(X,P,t)dt = K_q \cos\Big[k_q\Big(P\sin 2\pi\theta_q + X\cos 2\pi\theta_q\Big) - \phi_q\Big]. \tag{A6}$$

The above derivation is for classical dynamics. For quantum dynamics, the result has the same form with replacing X and P by their operators[15,59]. Extending the result for single kick to all kicks in Eq. (A1), we obtain the general form of phase-space lattice Hamiltonian

$$H_s(X,P) = \sum_q K_q \cos\Big[k_q\Big(P\sin 2\pi\theta_q + X\cos 2\pi\theta_q\Big) - \phi_q\Big]. \tag{A7}$$

In principle, any arbitrary lattice Hamiltonian in phase space can be synthesized by multiple stroboscopic lattices.

2. Honeycomb phase space lattice

For the honeycomb lattice considered in our work, we can get the desired driving parameters by decomposing the honeycomb lattice into a series of cosine functions and comparing the series expansion to Eq. (A7). It is straightforward to check that the kicking sequence given by the first three lines of parameter table in Fig. 2 generates the honeycomb lattice Hamiltonian in form of

$$H_s(\boldsymbol{Z}) = -\frac{16}{9}\omega_0\prod_{n=1}^{3}\sin^2\big(\frac{1}{2}\boldsymbol{v}_n\cdot\boldsymbol{Z}\big) - \frac{3}{2}\Lambda, \tag{A8}$$

where we have defined the vector $\boldsymbol{Z}\equiv(X,P)$ and three ancillary vectors $\boldsymbol{v}_1 = (\frac{2\sqrt{3}}{3},0)$, $\boldsymbol{v}_2 = (-\frac{\sqrt{3}}{3},1)$, $\boldsymbol{v}_3 = (-\frac{\sqrt{3}}{3},-1)$. The extrema of $H_s(X,P)$ represent stable points of the classical dynamics. The small vibrations about these stable points have frequency $\omega_0 = -9\Lambda$ from the linear expansion of Eq. (A8). The two sublattices of the phase-space honeycomb lattice Hamiltonian (A8) have the same vibration frequency at their lattice sites.

One can also tune the on-site frequencies of two sublattices with the following phase space lattice Hamiltonian

$$H_s^\Delta = -\frac{2\Delta}{\sqrt{3}}\sum_{n=1}^{3}\sin\big(\boldsymbol{v}_n\cdot\boldsymbol{Z}\big) = \frac{2\Delta}{\sqrt{3}}\sum_{n=1}^{3}\cos\big(\boldsymbol{v}_n\cdot\boldsymbol{Z} - \frac{3\pi}{2}\big), \tag{A9}$$

which can be implemented by additional stroboscopic lattices with kicking parameters $K_q = 2\Delta/\sqrt{3}$, $k_q = 2/\sqrt{3}$ and $\phi_q = 3\pi/2$ for $\theta_q = 1/12, 5/12, 9/12$ as listed by the fourth line of parameter table in Fig. 2. The on-site frequencies of two sublattices are then $\omega_0 \pm 2\Delta$ with the on-site detuning paramter Δ. The total single-particle Hamiltonian of honeycomb lattice is

$$H_s(\boldsymbol{Z}) = \frac{1}{2}\delta\omega|\boldsymbol{Z}|^2 - \frac{16}{9}\omega_0\prod_{n=1}^{3}\sin^2\big(\frac{1}{2}\boldsymbol{v}_n\cdot\boldsymbol{Z}\big) - \frac{2\Delta}{\sqrt{3}}\sum_{n=1}^{3}\sin\big(\boldsymbol{v}_n\cdot\boldsymbol{Z}\big). \tag{A10}$$

Here we have also included the global detuning $\delta\omega$ introduced in Eq. (A5).

Appendix B: Many-body Hamiltonian

We consider many interacting particles trapped in the same 1D harmonic potential. The interaction $V(x_i - x_j)$ induces an effective interaction of two particles on their quadratures[15,33–35]. The general method to extract this effective interaction in phase space has been developed in Refs.[15,35]. The interaction of cold atoms due to the s-wave scattering is a point-like contact interaction $V(x_i - x_j) = \gamma\delta(x_i - x_j)$. The effective phase-space interaction potential is a Coulomb-like interaction $U(R_{ij}) = \gamma\pi^{-1}R_{ij}^{-1}$, where

$$R_{ij} \equiv \sqrt{(X_i - X_j)^2 + (P_i - P_j)^2} = \Big|\boldsymbol{Z}_i - \boldsymbol{Z}_j\Big|$$

is the phase-space distance between two atoms i and j. The effective phase space interaction is valid for well-separated atoms which is the case of phase space crystals considered in this work[15,35]. Finally, we have the many-body Hamiltonian for this work

$$H = \sum_L H_s(X_L,P_L) + \frac{1}{2}\sum_{L\neq L'}U(R_{LL'}) \equiv T + \Phi. \tag{B1}$$

Here, we have relabelled the atoms by the subscript $L = (l,s)$ representing the l-th atom in the $s\in\{A,B\}$ sublattice. $T \equiv \sum_L H_s(X_L,P_L)$ is the total single-particle contribution and $\Phi \equiv \frac{1}{2}\sum_{L\neq L'}U(R_{LL'})$ othe total interaction part.

1. Equilibrium configuration

In the presence of the lattice potential and their effective interaction, the atoms have equilibrium configuration in phase space. The equilibrium points of atoms $\boldsymbol{Z}_L^0 = (X_L^0, P_L^0)$ are determined by the condition

$$\frac{\partial H}{\partial X_L}\bigg|_{(X_L^0,P_L^0)} = 0, \quad \frac{\partial H}{\partial P_L}\bigg|_{(X_L^0,P_L^0)} = 0, \tag{B2}$$

where H is the many-body Hamiltonian (B1). For the periodic boundaries in both X and P directions, the interactions from symmetric directions cancel each other

and the equilibrium points are given by the honeycomb lattice sites. The periodic boundary is helpful for theoretical study. In the real experimental setup, however, the equilibrium positions of atoms will deviate from the lattice sites due to the open boundary of phase space crystal. In fact, the atoms tend to relax towards the stable points and concentrate about the origin of the phase space due to the presence of dissipation. By introducing a relative strong repulsive interaction ($\gamma > 0$), the atoms will spread over the phase space and form a disk-shaped crystal state as shown by Fig. 1(c) in the main text. Note that the interaction of the atoms on the disk will tend to distort the honeycomb equilibrium configuration. There is a mean-field potential induced by the interaction. The effective potential generated by the disk crystal in phase space can be approximated by the Coulomb potential on a uniformly charged disk plane given by Eq.(7), and can be significantly counter-balanced by choosing the appropriate detuning $\delta\omega = 1.35\sigma\pi R^{-1}|\boldsymbol{Z}|^2/2$ in the single-particle Hamiltonian (A10) as discussed in Sec. III A.

2. Linearised Hamiltonian

We expand the total many-body Hamiltonian (B1) around the equilibrium positions of atoms, i.e., $\boldsymbol{Z}_L(t) = \boldsymbol{Z}_L^0 + \boldsymbol{u}_L(t)$ where $\boldsymbol{u}_L = (u_L^X, u_L^P)$ is the displacement on the lattice site L. To the second order, the many-body Hamiltonian is given by (up to a constant)

$$H = \frac{1}{2}\sum_{\alpha,\beta}\sum_{L,L'}\eta_{\alpha\beta}^{LL'}u_L^\alpha u_{L'}^\beta \tag{B3}$$

with the matrix $\eta_{\alpha\beta}^{LL'}$ given by

$$\eta_{\alpha\beta}^{LL'} = \left.\frac{\partial^2 H}{\partial u_L^\alpha \partial u_{L'}^\beta}\right|_{\mathbf{0}} = T_{\alpha\beta}^{LL'} + \Phi_{\alpha\beta}^{LL'}. \tag{B4}$$

We call $\eta_{\alpha\beta}^{LL'}$ the *phase space force matrix*, which means the resultant force along α direction exerted on the L-th atom due to the unit displacement along β direction of the L'-th atom. The contribution to $\eta_{\alpha\beta}^{LL'}$ from the single-particle Hamiltonian (A10) is

$$\begin{aligned} T_{\alpha\beta}^{LL'} &= \left.\frac{\partial^2 H_s}{\partial u_L^\alpha \partial u_{L'}^\beta}\right|_{\mathbf{0}} = \left.\frac{\partial^2 H_s}{\partial u_L^\alpha \partial u_L^\beta}\right|_{\mathbf{0}}\delta_{LL'} \\ &= T_{\alpha\beta}^{LL}\delta_{LL'} = (\omega_0 \pm 2\Delta)\delta_{\alpha\beta}\delta_{LL'}. \end{aligned} \tag{B5}$$

The contribution from interaction part can be obtained by calculating the derivative of interaction potential

$$\frac{\partial\Phi}{\partial Z_L^\alpha} = \sum_{L'\neq L}\frac{U'\big(R_{LL'}\big)}{R_{LL'}}\Big[(X_L - X_{L'})\delta_{X\alpha} + (P_L - P_{L'})\delta_{P\alpha}\Big]. \tag{B6}$$

For two different atoms at different lattice sites ($L \neq L'$), we have the second derivative

$$\begin{aligned} \Phi_{\alpha\beta}^{LL'} = \frac{\partial^2\Phi}{\partial Z_L^\alpha \partial Z_{L'}^\beta} &= \frac{U'\big(R_{LL'}\big)}{R_{LL'}}\big(-\delta_{X\alpha}\delta_{X\beta} - \delta_{P\alpha}\delta_{P\beta}\big) + \frac{U''\big(R_{LL'}\big)R_{LL'} - U'\big(R_{LL'}\big)}{R_{LL'}^3} \\ &\times\Big[-(X_L - X_{L'})\delta_{X\beta} - (P_L - P_{L'})\delta_{P\beta}\Big]\Big[(X_L - X_{L'})\delta_{X\alpha} + (P_L - P_{L'})\delta_{P\alpha}\Big]. \end{aligned} \tag{B7}$$

For the atom at the single lattice site ($L = L'$), we have the second derivative

$$\begin{aligned} \Phi_{\alpha\beta}^{LL} = \frac{\partial^2\Phi}{\partial Z_L^\alpha \partial Z_L^\beta} &= \sum_{L'\neq L}\frac{U'\big(R_{LL'}\big)}{R_{LL'}}\big(\delta_{X\alpha}\delta_{X\beta} + \delta_{P\alpha}\delta_{P\beta}\big) + \frac{U''\big(R_{LL'}\big)R_{LL'} - U'\big(R_{LL'}\big)}{R_{LL'}^3} \\ &\times\big[(X_L - X_{L'})\delta_{X\beta} + (P_L - P_{L'})\delta_{P\beta}\big]\big[(X_L - X_{L'})\delta_{X\alpha} + (P_L - P_{L'})\delta_{P\alpha}\big] \\ &= \sum_{L'\neq L}(-1)\times\frac{\partial^2\Phi}{\partial Z_{L'}^\beta \partial Z_L^\alpha}. \end{aligned} \tag{B8}$$

We introduce the complex field at each lattice site $a_L(t) \equiv \frac{1}{\sqrt{2\lambda}}\big[u_L^X(t) + iu_L^P(t)\big]$, where $\lambda = \hbar k^2/m\omega_{ax}$ is the dimensionless Planck constant, and obtain the Hamiltonian from Eq. (B3)

$$\mathcal{H}/\lambda = \sum_{L,L'} h_{LL'}a_L^\dagger a_{L'} + \frac{1}{2}g_{LL'}a_L^\dagger a_{L'}^\dagger + \frac{1}{2}g_{L'L}^* a_L a_{L'}. \tag{B9}$$

Here, h_{LL} represents the onsite energy of one excitation on L-th lattice site, $h_{LL'}(L \neq L')$ represents the hopping coefficient from L'-th lattice site to L-th lattice site, and $g_{LL'}$ represents pairing coefficient of creating or annihilating two phase-space phonons on the L-th and L'-th lattice sites. These coefficients are given by the phase space force matrix

$$\begin{cases} h_{LL'} \equiv \frac{1}{2}\big(\eta_{XX}^{LL'} + \eta_{PP}^{LL'}\big) + i\frac{1}{2}\big(\eta_{PX}^{LL'} - \eta_{XP}^{LL'}\big) \\ g_{LL'} \equiv \frac{1}{2}\big(\eta_{XX}^{LL'} - \eta_{PP}^{LL'}\big) + i\frac{1}{2}\big(\eta_{PX}^{LL'} + \eta_{XP}^{LL'}\big). \end{cases} \quad \text{(B10)}$$

From the property $\eta_{\alpha\beta}^{LL'} = \eta_{\beta\alpha}^{L'L}$, we have $h_{LL'} = h_{L'L}^*$ and $g_{LL'} = g_{L'L}$. Note that, compared to the Hamiltonian Eq. (5) in the main text, we have replaced the variable α_L by $a_L = \alpha_L/\sqrt{\lambda}$ in the Hamiltonian Eq. (B9). In the linearised regime, these two descriptions are equivalent to each other, but the Hamiltonian Eq. (B9) here bears the advantage that it can be directly translated into the second-quantized description by taking a_L as the ladder operator on the L-th lattice site, which makes the connection to other models, specifically the Haldane model[3], more transparent.

Below, we calculate the explicit form of $h_{LL'}$ and $g_{LL'}$ for the case of Coulomb-type interaction $U(R_{LL'}) = \gamma\pi^{-1}R_{LL'}^{-1}$. For the off-site ($L \neq L'$) coefficients, we have the hopping coefficients

$$\begin{aligned} h_{LL'} &= -\frac{U'\big(R_{LL'}\big)}{R_{LL'}} - \frac{1}{2}\frac{U''\big(R_{LL'}\big)R_{LL'} - U'\big(R_{LL'}\big)}{R_{LL'}} \\ &= -\frac{1}{2}\frac{U''\big(R_{LL'}\big)R_{LL'} + U'\big(R_{LL'}\big)}{R_{LL'}} \\ &= -\frac{\gamma}{2\pi R_{LL'}^3} \end{aligned} \quad \text{(B11)}$$

and the pairing coefficients

$$\begin{aligned} g_{LL'} &= -\frac{1}{2}\frac{U''\big(R_{LL'}\big)R_{LL'} - U'\big(R_{LL'}\big)}{R_{LL'}^3} \\ &\quad \times\Big[(X_L - X_{L'})^2 - (P_L - P_{L'})^2 \\ &\quad + i2(X_L - X_{L'})(P_L - P_{L'})\Big] \\ &= -\frac{1}{2}\frac{U''\big(R_{LL'}\big)R_{LL'} - U'\big(R_{LL'}\big)}{R_{LL'}}e^{i2\varphi_{LL'}} \\ &= -\frac{3\gamma}{2\pi R_{LL'}^3}e^{i2\varphi_{LL'}}, \end{aligned} \quad \text{(B12)}$$

where the phase parameter $\varphi_{LL'}$ is defined via

$$\begin{cases} X_L - X_{L'} = R_{LL'}\cos\varphi_{LL'}, \\ P_L - P_{L'} = R_{LL'}\sin\varphi_{LL'}. \end{cases} \quad \text{(B13)}$$

For the on-site ($L = L'$) coefficients, we have the on-site energy

$$\begin{aligned} \omega_L &\equiv h_{LL} \\ &= \frac{1}{2}(T_{XX}^{LL} + T_{PP}^{LL}) - \frac{1}{2}\sum_{L'\neq L}(\Phi_{XX}^{LL'} + \Phi_{PP}^{LL'}) \\ &= \frac{1}{2}(T_{XX}^{LL} + T_{PP}^{LL}) \\ &\quad + \frac{1}{2}\sum_{L'\neq L}\frac{U''\big(R_{LL'}\big)R_{LL'} + U'\big(R_{LL'}\big)}{R_{LL'}} \\ &= \frac{1}{2}(T_{XX}^{LL} + T_{PP}^{LL}) + \sum_{L'\neq L}\frac{\gamma}{2\pi R_{LL'}^3}. \end{aligned} \quad \text{(B14)}$$

and the squeezing rates

$$\begin{aligned} g_L &\equiv g_{LL} \\ &= \frac{1}{2}(T_{XX}^{LL} - T_{PP}^{LL}) + iT_{PX}^{LL} + \sum_{L'\neq L}\frac{3\gamma}{2\pi R_{LL'}^3}e^{i2\varphi_{LL'}}. \end{aligned} \quad \text{(B15)}$$

The above expressions are valid for any boundary condition and arbitrary single-particle Hamiltonian. Finally, we obtain the Hamiltonian of phase-space lattice waves

$$\begin{aligned} \frac{\mathcal{H}}{\lambda} &= \sum_L \omega_L a_L^\dagger a_L + \frac{1}{2}g_L a_L^{\dagger 2} + \frac{1}{2}g_L^* a_L^2 \\ &\quad - \frac{\gamma}{4\pi}\Bigg(\sum_{L\neq L'}\frac{a_L^\dagger a_{L'} + 3e^{i2\varphi_{LL'}}a_L^\dagger a_{L'}^\dagger}{|\mathbf{Z}_L^0 - \mathbf{Z}_{L'}^0|^3} + h.c.\Bigg). \end{aligned} \quad \text{(B16)}$$

For the honeycomb single-particle Hamiltonian (A10) and periodic boundary conditions, we have the simplified results of on-site coefficients

$$\omega_L = \omega_0 \pm 2\Delta + \sum_{L'\neq L}\frac{\gamma}{2\pi R_{LL'}^3}, \quad g_L = 0, \quad \text{(B17)}$$

where the summation in Eq. (B15) disappears due to the honeycomb lattice symmetry. The Hamiltonian Eq. (B16) describes phonons propagating in our honeycomb phase-space crystal. It is reminiscent of the tight-binding model for electrons in graphene but our phase-space phonons can hop between any two arbitrarily distant sites reflecting the long-range nature of the atom-atom interaction.

3. Pairing-induced staggered magnetic field

In order to better distinguish the effects of the (long-range) hopping and the pairing interaction, it is instructive to first consider a regime where the latter is suppressed, i.e., the creation of phonon pairs is far off-resonant $|\gamma| \ll |\omega_0|$. In this case, we can cancel the pairing-interaction terms in the Hamiltonian (B9) using the following unitary transformation

$$U \equiv \exp\Big(\sum_{\bar{L},\bar{L}'}\xi_{\bar{L}\bar{L}'}a_{\bar{L}}^\dagger a_{\bar{L}'}^\dagger - \xi_{\bar{L}'\bar{L}}^* a_{\bar{L}}a_{\bar{L}'}\Big) \equiv e^Y. \quad \text{(B18)}$$

It can be checked that $U^\dagger = e^{-Y}$ and thus $U^\dagger U = 1$. Using the following identities

$$\begin{aligned}
\big[a_L^\dagger a_{L'}, a_{\bar{L}}^\dagger a_{\bar{L}'}^\dagger\big] &= a_L^\dagger a_{\bar{L}'}^\dagger \delta_{L'\bar{L}} + a_L^\dagger a_{\bar{L}}^\dagger \delta_{L'\bar{L}'} \\
\big[a_L^\dagger a_{L'}, a_{\bar{L}} a_{\bar{L}'}\big] &= -a_{\bar{L}'} a_{L'} \delta_{L\bar{L}} - a_{\bar{L}} a_{L'} \delta_{L\bar{L}'} \\
\big[a_L^\dagger a_{L'}^\dagger, a_{\bar{L}} a_{\bar{L}'}\big] &= -a_L^\dagger a_{\bar{L}'} \delta_{L'\bar{L}} - a_L^\dagger a_{\bar{L}} \delta_{L'\bar{L}'} \\
&\quad -a_{\bar{L}'} a_{L'}^\dagger \delta_{L\bar{L}} - a_{\bar{L}} a_{L'}^\dagger \delta_{L\bar{L}'} \\
\big[a_L a_{L'}, a_{\bar{L}}^\dagger a_{\bar{L}'}^\dagger\big] &= a_L a_{\bar{L}}^\dagger \delta_{L'\bar{L}'} + a_L a_{\bar{L}'}^\dagger \delta_{L'\bar{L}} \\
&\quad + a_{\bar{L}'}^\dagger a_{L'} \delta_{L\bar{L}} + a_{\bar{L}}^\dagger a_{L'} \delta_{L\bar{L}'},
\end{aligned} \tag{B19}$$

we obtain

$$\begin{aligned}
\big[a_L^\dagger a_{L'}, Y\big] &= \sum_{\bar{L}} \tilde{\xi}_{\bar{L}L'} a_L^\dagger a_{\bar{L}'}^\dagger + \tilde{\xi}_{\bar{L}L}^* a_{\bar{L}} a_{L'}, \\
\big[a_L^\dagger a_{L'}^\dagger, Y\big] &= \sum_{\bar{L}} \tilde{\xi}_{\bar{L}L'}^* a_L^\dagger a_{\bar{L}} + \tilde{\xi}_{\bar{L}L}^* a_{\bar{L}} a_{L'}^\dagger, \\
\big[a_L a_{L'}, Y\big] &= \sum_{\bar{L}} \tilde{\xi}_{\bar{L}L'} a_L a_{\bar{L}}^\dagger + \tilde{\xi}_{\bar{L}L} a_{\bar{L}}^\dagger a_{L'},
\end{aligned} \tag{B20}$$

where we have defined $\tilde{\xi}_{\bar{L}L'} \equiv \xi_{\bar{L}L'} + \xi_{L'\bar{L}}$ with $\tilde{\xi}_{\bar{L}L'} = \tilde{\xi}_{L'\bar{L}}$. The Hamiltonian transformed by U to the leading order

$$U^\dagger \mathcal{H} U/\lambda = \mathcal{H}/\lambda + \big[\mathcal{H}/\lambda, Y\big] + \cdots \tag{B21}$$

where we have used the Hausdorff expansion

$$e^{-Y}\mathcal{H}e^{Y} = \mathcal{H} + [\mathcal{H}, Y] + \frac{1}{2!}[[\mathcal{H}, Y], Y] + \cdots .$$

The leading-order correction is

$$\begin{aligned}
\big[\mathcal{H}/\lambda, Y\big] &= \sum_{L;L';\bar{L}} h_{LL'} \xi_{\bar{L}L'} a_{ls}^\dagger a_{\bar{L}'}^\dagger + h_{LL'} \xi_{\bar{L}L}^* a_{\bar{L}} a_{L'} \\
&\quad + \frac{1}{2} g_{LL'} \tilde{\xi}_{\bar{L}L'}^* a_L^\dagger a_{\bar{L}} + \frac{1}{2} g_{LL'} \tilde{\xi}_{\bar{L}L}^* a_{\bar{L}} a_{L'}^\dagger \\
&\quad + \frac{1}{2} g_{L'L}^* \tilde{\xi}_{\bar{L}L'} a_L a_{\bar{L}}^\dagger + \frac{1}{2} g_{L'L}^* \tilde{\xi}_{\bar{L}L} a_{\bar{L}}^\dagger a_{L'} \\
&= \sum_{L;L'} \tilde{h}_{LL'} a_L^\dagger a_{L'} + \frac{1}{2} \tilde{g}_{LL'} a_L^\dagger a_{L'}^\dagger + \frac{1}{2} \tilde{g}_{L'L}^* a_L a_{L'}.
\end{aligned} \tag{B22}$$

Neglecting constants from $a_L a_L^\dagger = a_L^\dagger a_L + 1$ and using the symmetry property $g_{LL'} = g_{L'L}$, we have the coefficients

$$\begin{aligned}
\tilde{h}_{LL'} &= \sum_{\bar{L}} g_{\bar{L}L'}^* \tilde{\xi}_{\bar{L}L} + g_{L\bar{L}} \tilde{\xi}_{\bar{L}L'}^*, \\
\tilde{g}_{LL'} &= \sum_{\bar{L}} h_{L\bar{L}} \tilde{\xi}_{\bar{L}L'}, \\
\tilde{g}_{L'L}^* &= \sum_{\bar{L}} h_{\bar{L}L'} \tilde{\xi}_{\bar{L}L}^*.
\end{aligned} \tag{B23}$$

To cancel the pairing terms in the Hamiltonian (B9), it needs $g_{LL'} + \tilde{g}_{LL'} = 0$, i.e.,

$$g_{LL'} = -\sum_{\bar{L}} h_{L\bar{L}} \tilde{\xi}_{\bar{L}L'}. \tag{B24}$$

We make the assumption that the on-site energy is much larger than the off-site hopping terms, i.e., $\omega_L \equiv h_{LL} \gg h_{L\bar{L}}$ with $L \neq \bar{L}$, which results in

$$\tilde{\xi}_{LL'} \approx -\frac{g_{LL'}}{\omega_L} \quad \Longrightarrow \quad \xi_{LL'} = \xi_{L'L} = -\frac{g_{LL'}}{2\omega_L}.$$

Finally, we have the pairing-induced hopping rate

$$\tilde{h}_{LL'} \approx -\sum_{\bar{L}} \frac{2}{\omega_{\bar{L}}} g_{L\bar{L}} g_{\bar{L}L'}^*. \tag{B25}$$

Note that the pairing-induced hopping is proportional to the square of interaction strength $|\tilde{h}_{L\bar{L}}| \propto \gamma^2/\omega_0$. Considering the case beyond NN interaction, there is a direct real-valued hopping rate between lattice sites L and $\bar{L}$, which is proportional to the interaction strength $h_{L\bar{L}} \propto \gamma$. As a result, the pairing-induced non-reciprocal hopping pathway $\tilde{h}_{L\bar{L}}$ interferes with a direct hopping pathway $h_{L\bar{L}}$ leads to a weak staggered magnetic flux of the order $\Phi \sim \gamma/\omega_0$. This is the essential ingredients of Haldane model[3], which introduces a staggered magnetic field breaking the time-reversal symmetry inside each unit cell but leaving the total net flus through the unit cell zero.

Our model recovers the anomalous quantum Hall effect similar to the Haldane model only in the weak off-resonant interaction regime. Our effective particle-conserving description (which is derived from a perturbation theory in γ/ω_0) differs from the Haldane model in that it includes long-range hopping transitions. For sufficiently strong interaction (non-perturbative regime), our model has some new features which do not appear in Haldane model, e.g., new topological phase regime and the lost of stability.

Appendix C: Topological Band Structure

1. Periodic boundary condition

For periodic boundaries both in X and P directions, we Fourier transform the linearised Hamiltonian (B9) using

$$\begin{cases} a_{l,s} = \frac{1}{\sqrt{N}} \sum_{\boldsymbol{k}} a_{\boldsymbol{k},s} \exp(i\boldsymbol{k} \cdot \boldsymbol{Z}_{l,s}^0); \\ a_{l,s}^\dagger = \frac{1}{\sqrt{N}} \sum_{\boldsymbol{k}} a_{\boldsymbol{k},s}^\dagger \exp(-i\boldsymbol{k} \cdot \boldsymbol{Z}_{l,s}^0), \end{cases} \tag{C1}$$

where $\boldsymbol{k} = (k_X, k_P)$, $Z_{l,s}^0$ is the equilibrium position of atom $L = (l, s)$ and N is the total number of unite cells. The operators from inverse Fourier transformation

$$\begin{cases} a_{\boldsymbol{k},s} = \frac{1}{\sqrt{N}} \sum_{l} a_{l,s} \exp(-i\boldsymbol{k} \cdot \boldsymbol{Z}_{l,s}^0); \\ a_{\boldsymbol{k},s}^\dagger = \frac{1}{\sqrt{N}} \sum_{l} a_{l,s}^\dagger \exp(i\boldsymbol{k} \cdot \boldsymbol{Z}_{l,s}^0), \end{cases} \tag{C2}$$

satisfy the commutation of Bosons, i.e.,

$$[a_{\boldsymbol{k},s}, a_{\boldsymbol{k}',s'}^\dagger] = \delta_{\boldsymbol{k}\boldsymbol{k}'} \delta_{ss'}; \;\; [a_{\boldsymbol{k},s}, a_{\boldsymbol{k}',s'}] = 0. \tag{C3}$$

The hopping terms in the Hamiltonian (B9) become

$$\begin{aligned}
&\sum_{l,l'} h_{(l,s),(l',s')} a^\dagger_{l,s} a_{l',s'} \\
&= \frac{1}{N}\sum_{\boldsymbol{k},\boldsymbol{k}'} a^\dagger_{\boldsymbol{k},s} a_{\boldsymbol{k}',s'} \\
&\quad \times \sum_{l,l'} h_{(l,s),(l',s')} e^{-i\boldsymbol{k}\cdot(\boldsymbol{Z}^0_{l,s}-\boldsymbol{Z}^0_{l',s'})-i(\boldsymbol{k}-\boldsymbol{k}')\cdot\boldsymbol{Z}^0_{l',s'}} \\
&\equiv \sum_{\boldsymbol{k}} h_{s,s'}(\boldsymbol{k}) a^\dagger_{\boldsymbol{k},s} a_{\boldsymbol{k},s'} \qquad \text{(C4)}
\end{aligned}$$

with the definition of hopping coefficients in reciprocal $\boldsymbol{k} = (k_X, k_P)$ space

$$h_{s,s'}(\boldsymbol{k}) \equiv \sum_l h_{(l,s),(l',s')} \exp[-i\boldsymbol{k}\cdot(\boldsymbol{Z}^0_{l,s} - \boldsymbol{Z}^0_{l',s'})]. \quad \text{(C5)}$$

We find the property $h^*_{s,s'}(\boldsymbol{k}) = h_{s',s}(\boldsymbol{k})$ using the identity $h_{(l,s),(l',s')} = h^*_{(l',s'),(l,s)}$ and the discrete translational lattice symmetry. Similarly, the pairing terms in the Hamiltonian (B9) become

$$\begin{aligned}
&\sum_{l,l'} g_{(l,s),(l',s')} a^\dagger_{l,s} a^\dagger_{l',s'} \\
&= \frac{1}{N}\sum_{\boldsymbol{k},\boldsymbol{k}'} a^\dagger_{\boldsymbol{k},s} a^\dagger_{\boldsymbol{k}',s'} \\
&\quad \times \sum_{l,l'} g_{(l,s),(l',s')} e^{-i\boldsymbol{k}\cdot(\boldsymbol{Z}^0_{l,s}-\boldsymbol{Z}^0_{l',s'})-i(\boldsymbol{k}+\boldsymbol{k}')\cdot\boldsymbol{Z}^0_{l',s'}} \\
&= \sum_{k} g_{s,s'}(\boldsymbol{k}) a^\dagger_{k,s} a^\dagger_{-k,s'} \qquad \text{(C6)}
\end{aligned}$$

with the definition of pairing coefficient in reciprocal $\boldsymbol{k} = (k_X, k_P)$ space

$$g_{s,s'}(\boldsymbol{k}) \equiv \sum_l g_{(l,s),(l',s')} \exp[-i\boldsymbol{k}\cdot(\boldsymbol{Z}^0_{l,s} - \boldsymbol{Z}^0_{l',s'})]. \quad \text{(C7)}$$

We find the property $g_{s,s'}(-\boldsymbol{k}) = g_{s',s}(\boldsymbol{k})$ using the identity $g_{(l,s),(l',s')} = g_{(l',s'),(l,s)}$ and the discrete lattice translational symmetry. As a result, the Hamiltonian in the reciprocal space is given by

$$\begin{aligned}
\mathcal{H}/\lambda &= \sum_{\boldsymbol{k},s,s'} h_{s,s'}(\boldsymbol{k}) a^\dagger_{\boldsymbol{k},s} a_{\boldsymbol{k},s'} \\
&\quad + \frac{1}{2} g_{s,s'}(\boldsymbol{k}) a^\dagger_{\boldsymbol{k},s} a^\dagger_{-\boldsymbol{k},s'} + \frac{1}{2} g^*_{s,s'}(\boldsymbol{k}) a_{-\boldsymbol{k},s'} a_{\boldsymbol{k},s} \\
&= \sum_{\boldsymbol{k}} \boldsymbol{A}^T_{\boldsymbol{k}} \mathcal{H}_{\boldsymbol{k}} \boldsymbol{A}_{\boldsymbol{k}}, \qquad \text{(C8)}
\end{aligned}$$

where we have deined the vector $\boldsymbol{A}_{\boldsymbol{k}} \equiv (a_{\boldsymbol{k},A},\ a_{\boldsymbol{k},B},\ a^\dagger_{-\boldsymbol{k},A},\ a^\dagger_{-\boldsymbol{k},B})^T$ and the Bogoliubov-de-Gennes (BdG) Hamiltonian

$$\mathcal{H}_{\boldsymbol{k}} \equiv \begin{pmatrix} h_{A,A}(\boldsymbol{k}) & h_{A,B}(\boldsymbol{k}) & \frac{1}{2}g_{A,A}(\boldsymbol{k}) & \frac{1}{2}g_{A,B}(\boldsymbol{k}) \\ h_{B,A}(\boldsymbol{k}) & h_{B,B}(\boldsymbol{k}) & \frac{1}{2}g_{B,A}(\boldsymbol{k}) & \frac{1}{2}g_{B,B}(\boldsymbol{k}) \\ \frac{1}{2}g^*_{A,A}(\boldsymbol{k}) & \frac{1}{2}g^*_{A,B}(\boldsymbol{k}) & h_{A,A}(-\boldsymbol{k}) & h_{A,B}(-\boldsymbol{k}) \\ \frac{1}{2}g^*_{B,A}(\boldsymbol{k}) & \frac{1}{2}g^*_{B,B}(\boldsymbol{k}) & h_{B,A}(-\boldsymbol{k}) & h_{B,B}(-\boldsymbol{k}) \end{pmatrix}.$$

From the Heisenberg equation

$$\begin{aligned}
-i\frac{d}{dt}a_{\boldsymbol{k},s} &= \frac{1}{\lambda}[\mathcal{H}, a_{\boldsymbol{k},s}] \\
&= \sum_{s'} -h_{s,s'}(\boldsymbol{k}) a_{\boldsymbol{k},s'} \\
&\quad -\frac{1}{2} g_{s,s'}(\boldsymbol{k}) a^\dagger_{-\boldsymbol{k},s'} - \frac{1}{2} g_{s',s}(-\boldsymbol{k}) a^\dagger_{-\boldsymbol{k},s'},
\end{aligned}$$

we have the EOM for the ladder operator $\boldsymbol{A}_{\boldsymbol{k}}$ as following

$$i\frac{d}{dt}\boldsymbol{A}_{\boldsymbol{k}} = D(\boldsymbol{k})\boldsymbol{A}_{\boldsymbol{k}}. \qquad \text{(C9)}$$

Here $D(\boldsymbol{k})$ is the dynamical matrix defined by

$$D(\boldsymbol{k}) \equiv \begin{pmatrix} h_{A,A}(\boldsymbol{k}) & h_{A,B}(\boldsymbol{k}) & \bar{g}_{A,A}(\boldsymbol{k}) & \bar{g}_{A,B}(\boldsymbol{k}) \\ h_{B,A}(\boldsymbol{k}) & h_{B,B}(\boldsymbol{k}) & \bar{g}_{B,A}(\boldsymbol{k}) & \bar{g}_{B,B}(\boldsymbol{k}) \\ -\bar{g}^*_{A,A}(\boldsymbol{k}) & -\bar{g}^*_{B,A}(\boldsymbol{k}) & -h^*_{A,A}(-\boldsymbol{k}) & -h^*_{A,B}(-\boldsymbol{k}) \\ -\bar{g}^*_{A,B}(\boldsymbol{k}) & -\bar{g}^*_{B,B}(\boldsymbol{k}) & -h^*_{B,A}(-\boldsymbol{k}) & -h^*_{B,B}(-\boldsymbol{k}) \end{pmatrix}$$

wit the symmetric pairing coefficients dedined by

$$\bar{g}_{s,s'}(\boldsymbol{k}) \equiv \frac{1}{2}\Big[g_{s,s'}(\boldsymbol{k}) + g_{s',s}(-\boldsymbol{k})\Big].$$

The eigen solutions of EOM (C9) can be obtained by diagonalising the dynamical matrix $D(\boldsymbol{k})$. We label the frequency spectrum by $\omega_{\boldsymbol{k},n}$, where $n = 1, 2, 3, 4$ is the index of four bands. For each given $\boldsymbol{k}$ and band index n, the eigenstate is a four-component vector $|\boldsymbol{k}, n\rangle = (u_{n,A},\ u_{n,B},\ v_{n,A},\ v_{n,B})$. Then, the Hamiltonian can be cast into a diagonal form of

$$\mathcal{H}/\lambda = \sum_{\boldsymbol{k},n} \omega_{\boldsymbol{k},n} b^\dagger_{\boldsymbol{k},n} b_{\boldsymbol{k},n}, \qquad \text{(C10)}$$

where the normal modes are given by a Bogoliubov transformation in the form of

$$b^\dagger_{\boldsymbol{k},n} = \sum_{s=A,B} u_{n,s}(\boldsymbol{k}) a^\dagger_{\boldsymbol{k},s} + v_{n,s}(\boldsymbol{k}) a_{-\boldsymbol{k},s}.$$

From the property $\bar{g}_{s,s'}(\boldsymbol{k}) = \bar{g}_{s,s'}(-\boldsymbol{k})$, the dynamical matrix has *particle-hole symmetry* expressed by

$$\Xi D(\boldsymbol{k}) \Xi^{-1} = -D(-\boldsymbol{k}). \qquad \text{(C11)}$$

The particle-hole operator is defined via $\Xi = \tau_x K$ satisfies $\Xi^2 = +1$, where

$$\tau_x = \begin{pmatrix} 0 & 0 & 1 & 0 \\ 0 & 0 & 0 & 1 \\ 1 & 0 & 0 & 0 \\ 0 & 1 & 0 & 0 \end{pmatrix} \qquad \text{(C12)}$$

and K is the complex conjugation. It follows that each eigenmode at frequency $\omega(\boldsymbol{k})$ has a partner eigenmode at $-\omega(-\boldsymbol{k})$, namely, creating a quasiparticle in the state $\omega(\boldsymbol{k})$ has the same effect as removing one (creating a hole) from the state $-\omega(-\boldsymbol{k})$. Therefore, we label the two upper bands ($n = 1, 2$) as particle bands and two lower

bands ($n = 3, 4$) as the hole bands. From the bosonic commutation relationship $[b_{\boldsymbol{k}',n'}, b^\dagger_{\boldsymbol{k},n}] = \delta_{n,n'}\delta_{\boldsymbol{k}',\boldsymbol{k}}$, the eigenmodes have to follow the ortho-normal condition

$$\langle \boldsymbol{k}, n'|\Sigma_z|\boldsymbol{k}, n\rangle \equiv \sum_s u^*_{n',s}u_{n,s} - v^*_{n',s}v_{n,s} = \pm\delta_{n,n'}, \tag{C13}$$

where $\Sigma_z \equiv \mathrm{diag}(1, 1, -1, -1)$ is a 4×4 diagonal matrix and the positive (negative) sign corresponds to particle (hole) bands.

2. Symplectic Chern number

Different from the particle-conserving case, the ground state of the BdG Hamiltonian $\mathcal{H}_{\boldsymbol{k}}$ is a multi-mode squeezed state with non-zero phonon/photon number. By regarding the $\boldsymbol{k} = (k_X, k_P)$ as an external adiabatic parameter, we calculate the Berry phase accumulated by a single Bogoliubov quasi-particle in a specific n-th band along a closed loop covering the whole Brillouin zone (BZ), i.e.,

$$\begin{aligned}
\Phi_n &= i\oint_{BZ}\langle S_{\boldsymbol{k}}|b_{\boldsymbol{k},n}\nabla_{\boldsymbol{k}}b^\dagger_{\boldsymbol{k},n}|S_{\boldsymbol{k}}\rangle\cdot d\boldsymbol{k}\\
&= i\oint_{BZ}\langle S_{\boldsymbol{k}}|[b_{\boldsymbol{k},n}\nabla_{\boldsymbol{k}}b^\dagger_{\boldsymbol{k},n}]|S_{\boldsymbol{k}}\rangle\cdot d\boldsymbol{k} + i\oint_{BZ}\langle S_{\boldsymbol{k}}|\nabla_{\boldsymbol{k}}|S_{\boldsymbol{k}}\rangle\cdot d\boldsymbol{k}\\
&= i\oint_{BZ}\Big[\sum_s u^*_{n,s}(\boldsymbol{k})\nabla_{\boldsymbol{k}}u_{n,s}(\boldsymbol{k}) - v^*_{n,s}(\boldsymbol{k})\nabla_{\boldsymbol{k}}v_{n,s}(\boldsymbol{k})\Big]\cdot d\boldsymbol{k} + i\oint_{BZ}\langle S_{\boldsymbol{k}}|\nabla_{\boldsymbol{k}}|S_{\boldsymbol{k}}\rangle\cdot d\boldsymbol{k}\\
&\equiv \oint_{BZ}\mathcal{A}_n(\boldsymbol{k})\cdot d\boldsymbol{k} + \phi_n.
\end{aligned} \tag{C14}$$

Here, $|S_{\boldsymbol{k}}\rangle$ is the ground state (Bogoliubov vacuum state) of $\mathcal{H}_{\boldsymbol{k}}$ and, in the second line, we have used $b_{\boldsymbol{k},n}|S_{\boldsymbol{k}}\rangle = 0$ by the definition of vacuum state. Because of the unusual ortho-normalization (C13), we have updated the definition of the Berry connection by[8,39]

$$\mathcal{A}_n(\boldsymbol{k}) = i\langle \boldsymbol{k}, n|\Sigma_z\nabla_{\boldsymbol{k}}|\boldsymbol{k}, n\rangle. \tag{C15}$$

Note that the Berry connection defined here for the Bosonic many-body second-quantized Hamiltonian is different from the Berry connection for the single-particle Hamiltonian. The Bogoliubov vacuum $|S_{\boldsymbol{k}}\rangle$ depends on $\boldsymbol{k}$ and could possibly accumulate a Berry phase, i.e., $\phi_n \equiv i\oint\langle S_{\boldsymbol{k}}|\nabla_{\boldsymbol{k}}|S_{\boldsymbol{k}}\rangle\cdot d\boldsymbol{k} \neq 0$. However, the Berry phase of our interest is the additional Berry phase accumulated by the quasi-particle, i.e., the difference of Bogoliubov vacuum Berry phase and that associated with a single quasiparticle excitation. We thus update the definition of Chern number by[8,39]

$$C_n = \frac{1}{2\pi}\int_{BZ}\big(\nabla_{\boldsymbol{k}}\times\mathcal{A}_n(\boldsymbol{k})\big)\cdot\hat{\boldsymbol{n}} \in \mathbb{Z}, \tag{C16}$$

where $\hat{\boldsymbol{n}}$ is the unit vector normal to the $\boldsymbol{k}$-plane. Due to the additional element Σ_z in the Berry connection (C15), the quantity given by Eq. (C16) is also called *symplectic Chern number*. Since the quantum states come back to itself along a closed loop, the quantities Φ_n and ϕ_n are integers multiple of 2π, and thus the symplectic Chern number is also an integer.

As there is no net geometric phase (total flux of synthetic magnetic field) in our model, the sum of the Chern numbers over the particle bands must be zero. The Chern number of individual band may change after a phase transition where two or more bands touch each other, but their sum does not change. For this reason, we define the Chern number of the lowest band as the Chern number of our system $C = C_1$.

3. Strip boundary condition

For the periodic boundary in X direction but open boundary in P direction (strip boundary condition), we can only perform Fourier transformation in X direction

$$\begin{cases} a_{l,s} = \frac{1}{\sqrt{N_X}}\sum_{k_X} a_{k_X,(l_P,s)}\exp(ik_X X^0_{l,s}); \\ a^\dagger_{l,s} = \frac{1}{\sqrt{N_X}}\sum_{k_X} a^\dagger_{k_X,(l_P,s)}\exp(-ik_X X^0_{l,s}), \end{cases} \tag{C17}$$

where N_X is the number of unit cells in X direction and (l_P, s) labels the position of atoms in P direction. Then, the hopping terms in the Hamiltonian (B9) become

$$\begin{aligned}
&\sum_{l,l'} h_{(l,s),(l',s')}a^\dagger_{l,s}a_{l',s'}\\
&= \frac{1}{N_X}\sum_{l,l'}\sum_{k_X,k'_X} a^\dagger_{k_X,(l_P,s)}a_{k'_X,(l'_P,s')}\\
&\quad\times h_{(l,s),(l',s')}e^{-ik_X(X^0_{l,s}-X^0_{l',s'})-i(k_X-k'_X)X^0_{l',s'}}\\
&= \sum_{l_P,l'_P}\sum_{k_X} h_{(l_P,s),(l'_P,s')}(k_X)a^\dagger_{k_X,(l_P,s)}a_{k_X,(l'_P,s')}
\end{aligned} \tag{C18}$$

with the Fourier transformation of hopping coefficients

$$h_{(l_P,s),(l'_P,s')}(k_X) \equiv \sum_{l_X} h_{(l,s),(l',s')} e^{-ik_X\cdot(X^0_{l,s}-X^0_{l',s'})}, \tag{C19}$$

which has the property $h^*_{(l'_P,s'),(l_P,s)}(k_X) = h_{(l_P,s),(l'_P,s')}(k_X)$ using the identity $h_{(l,s),(l',s')} = h^*_{(l',s'),(l,s)}$ and discrete translational symmetry in X-direction. Similarly, the pairing terms in the Hamiltonian (B9) become

$$\begin{aligned}
&\sum_{l,l'} g_{s,s'}(l-l') a^\dagger_{l,s} a^\dagger_{l',s'} \\
&= \frac{1}{N_X}\sum_{l,l'}\sum_{k_X,k'_X} a^\dagger_{k_X,(l_P,s)} a^\dagger_{k'_X,(l'_P,s')} \\
&\quad \times g_{(l,s),(l',s')} e^{-ik_X(X^0_{l,s}-X^0_{l',s'})-i(k_X+k'_X)X^0_{l',s'}} \\
&= \sum_{l_P,l'_P}\sum_{k_X} g_{(l_P,s),(l'_P,s')}(k_X) a^\dagger_{k_X,(l_P,s)} a^\dagger_{-k_X,(l'_P,s')}
\end{aligned} \tag{C20}$$

with the Fourier transformation of pairing coefficients

$$g_{(l_P,s),(l'_P,s')}(k_X) \equiv \sum_{l_X} g_{(l,s),(l',s')}(l-l') e^{-ik_X\cdot(X^0_{l,s}-X^0_{l',s'})},$$

which has the property of $g_{(l_P,s),(l'_P,s')}(-k_X) = g_{(l'_P,s'),(l_P,s)}(k_X)$ using the identity $g_{(l,s),(l',s')} = g_{(l',s'),(l,s)}$ and discrete translational symmetry in X-direction. Therefore, the Hamiltonian in momentum space is

$$\begin{aligned}
\mathcal{H}/\lambda = &\sum_{l_P,l'_P}\sum_{k_X} h_{(l_P,s),(l'_P,s')}(k_X) a^\dagger_{k_X,(l_P,s)} a_{k_X,(l'_P,s')} \\
&+\frac{1}{2} g_{(l_P,s),(l'_P,s')}(k_X) a^\dagger_{k_X,(l_P,s)} a^\dagger_{-k_X,(l'_P,s')} \\
&+\frac{1}{2} g^*_{(l_P,s),(l'_P,s')}(k_X) a_{k_X,(l_P,s)} a_{-k_X,(l'_P,s')}
\end{aligned}$$

From the Heisenberg equation

$$\begin{aligned}
-i\frac{d}{dt} a_{k_X,(l_P,s)} = &\sum_{l'_P,s'} -h_{(l_P,s),(l'_P,s')}(k_X) a_{k_X,(l'_P,s')} \\
&-\frac{1}{2}[g_{(l_P,s),(l'_P,s')}(k_X) + g_{(l'_P,s'),(l_P,s)}(-k_X)] a^\dagger_{-k_X,(l'_P,s')},
\end{aligned} \tag{C21}$$

we have EOM for the operator $\boldsymbol{A}_{l_p}(k_X) \equiv (a_{k_X,(l_P,A)}, a_{k_X,(l_P,B)}, a^\dagger_{-k_X,(l_P,A)}, a^\dagger_{-k_X,(l_P,B)})^T$

$$i\frac{d}{dt}\begin{pmatrix} \boldsymbol{A}_1 \\ \vdots \\ \boldsymbol{A}_{l'_P} \\ \vdots \\ \boldsymbol{A}_{N_P} \end{pmatrix} = \begin{pmatrix} D_{(l_P=1,l'_P=1)} & \cdots & D_{(l_P=1,l'_P)} & \cdots & D_{(l_P=1,l'_P=N_P)} \\ \vdots & \ddots & \vdots & \vdots & \vdots \\ D_{(l_P,l'_P=1)} & \cdots & D_{l'_P,l_P} & \cdots & D_{(l_P,l'_P=N_P)} \\ \vdots & \vdots & \vdots & \ddots & \vdots \\ D_{(l_P=N_P,l'_P=1)} & \cdots & D_{(l_P=N_P,l'_P)} & \cdots & D_{(l_P=N_P,l'_P=N_P)} \end{pmatrix} \begin{pmatrix} \boldsymbol{A}_1 \\ \vdots \\ \boldsymbol{A}_{l'_P} \\ \vdots \\ \boldsymbol{A}_{N_P} \end{pmatrix},$$

where the block matrix element is given by

$$D_{(l_P,l'_P)}(k_X) \equiv \begin{pmatrix} h_{(l_P,A),(l'_P,A)}(k_X) & h_{(l_P,A),(l'_P,B)}(k_X) & \bar{g}_{(l_P,A),(l'_P,A)}(k_X) & \bar{g}_{(l_P,A),(l'_P,B)}(k_X) \\ h_{(l_P,B),(l'_P,A)}(k_X) & h_{(l_P,B),(l'_P,B)}(k_X) & \bar{g}_{(l_P,B),(l'_P,A)}(k_X) & \bar{g}_{(l_P,B),(l'_P,B)}(k_X) \\ -\bar{g}^*_{(l_P,A),(l'_P,A)}(-k_X) & -\bar{g}^*_{(l_P,A),(l'_P,B)}(-k_X) & -h^*_{(l_P,A),(l'_P,A)}(-k_X) & -h^*_{(l_P,A),(l'_P,B)}(-k_X) \\ -\bar{g}^*_{(l_P,B),(l'_P,A)}(-k_X) & -\bar{g}^*_{(l_P,B),(l'_P,B)}(-k_X) & -h^*_{(l_P,B),(l'_P,A)}(-k_X) & -h^*_{(l_P,B),(l'_P,B)}(-k_X) \end{pmatrix}$$

with the modified pairing coefficient

$$\bar{g}_{(l_P,s),(l'_P,s')}(k_X) \equiv \frac{1}{2}\Big[g_{(l_P,s),(l'_P,s')}(k_X) + g_{(l'_P,s'),(l_P,s)}(-k_X)\Big]. \tag{C22}$$

By extending the definition of operator τ_x in Eq. (C12) to all the matrix elements of $D(k_X)$ labelled by (l_P, l'_P) and using the property $\bar{g}_{(l_P,s),(l'_P,s')}(k_X) = \bar{g}_{(l_P,s),(l'_P,s')}(-k_X)$, the dynamical matrix $D_{(l_P,l'_P)}(k_X)$

has *particle-hole symmetry* expressed by

$$\Xi D_{(l_P,l'_P)}(k_X)\Xi^{-1} = -D_{(l_P,l'_P)}(-k_X), \quad \text{(C23)}$$

where the particle-hole operator is defined via $\Xi = \tau_x K$ satisfies $\Xi^2 = +1$. Again, we should diagonalise the dynamical matrix $D(k_X)$, instead of the Hamiltonian, to solve EOM and obtain the eigenmodes.

Appendix D: Experimental Conditions

1. Quasi-1D trapping potential

In order to create a quasi-1D harmonic potential for the cold atoms, one can start from a small Bose-Einstein condensate (BEC) in a magnetic trap[60]. Then, the BEC is loaded into a 2D optical potential, along y and z directions as shown by Fig. 1(b) in the main text, by superimposing two orthogonal standing waves on top of the BEC. Each standing wave is formed by two counter-propagating Gaussian laser beams. Supposing the laser light has wavelength (wave vector) λ_L ($k_L = 2\pi/\lambda_L$), the lattice potential has the form of $V(x,y,z) = V_0(\sin^2 ky + \sin^2 kz)$ with the potential depth V_0 laser intensity. As a result, an array of 1D quantum gases confined to narrow potential tubes is created. For a sufficiently strong potential depth (laser intensity), the tunnel coupling and particle exchange between different tubes are exponentially suppressed[32]. The Gaussian profile of the laser beams also leads to axial confinement of the quasi-1D gases. The resulting transverse (in the y-z plane) trapping frequency ω_{tr} and axial trapping frequency ω_{ax} are given by[61]

$$\omega_{tr} = \frac{2E_r}{\hbar}\sqrt{\frac{V_0}{E_r}}, \quad \omega_{ax} = \frac{\lambda_L}{\pi w_0}\omega_{tr}, \quad \text{(D1)}$$

where $E_r = \hbar^2 k_L^2/2m$ is the recoil energy of an atom with mass m, and w_0 is the Gaussian beam waist which sets the length of 1D harmonic trap.

2. Stroboscopic lattice potential

In our stroboscopic driving scheme, we need to control the stroboscopic lattice constant, which is usually much longer than the wavelength of laser lights. For this purpose, one can superimpose two equally polarized laser beams of wavelength λ_D intersecting at an angle θ as shown by Fig. 1(b) in the main text. The result is a standing wave optical dipole potential with a spatial period of[62]

$$d = \frac{\lambda_D}{2\sin(\theta/2)}. \quad \text{(D2)}$$

As discussed in Eq. (A10), we need three stroboscopic lattices with the ratio of lattice constants

$$d_1 : d_2 : d_3 = \frac{1}{2} : \frac{\sqrt{3}}{4} : \frac{\sqrt{3}}{2}$$

to create the honeycomb lattice. This can be achieved by either adjusting the angle θ of the same laser light or choosing three laser lights with different wavelengths λ_D.

3. Interaction

At the low temperature in ultracold atom experiments, the collision of cold atoms is dominated by s-wave scattering process. The two-body interactions of ultracold gases in 3D can be described by a pseudopotential in the form of contact function[32]

$$V_{3D}(\boldsymbol{r}) = \frac{4\pi\hbar^2 a}{2m}\delta(\boldsymbol{r}), \quad \text{(D3)}$$

where a is the s-wave scattering length. The scattering length a can be further tuned by the Feshbach resonance with a magnetic field B, i.e.,

$$a(B) = a_{bg}\big[1 - \frac{\Delta B}{B - B_0}\big]. \quad \text{(D4)}$$

Here, a_{bg} is the off-resonant background scattering length, while ΔB and B_0 describe the width and position of the resonance.

In the quasi-1D trap, the strength of contact interaction can be modified by the transverse mode. The effective pesodupotential is described by an interaction of the form[32]

$$V_{1D}(x) = \frac{2\hbar\omega_{tr}a}{1 - Aa/l_{tr}}\delta(x) \approx 2\hbar\omega_{tr}a\delta(x), \quad \text{(D5)}$$

where the constant $A = 1.036$ and $l_{tr} = \sqrt{\hbar/m\omega_{tr}}$ is the characteristic length of transverse motion. The approximation comes from the fact that the scattering length a is usually much shorter than the trapping length l_{tr}.

4. System size

During the collision, the kinetic energy of two atoms should not excite the transverse mode. This sets a restriction for the size (radius R) of phase space crystal,

$$2 \times \frac{1}{2}m\omega_{ax}^2\big(\frac{d}{2\pi}R\big)^2 < \hbar\omega_{tr} \quad \text{(D6)}$$

which results in the condition

$$R < \frac{2\pi}{d}\sqrt{\frac{\hbar\omega_{tr}}{m\omega_{ax}^2}} = \frac{2\pi}{d}\sqrt{\frac{\hbar\pi w_0}{m\lambda_L\omega_{ax}}}. \quad \text{(D7)}$$

[1] K. v. Klitzing, G. Dorda, and M. Pepper, "New method for high-accuracy determination of the fine-structure constant based on quantized hall resistance," Phys. Rev. Lett. **45**, 494 (1980).

[2] M. Z. Hasan and C. L. Kane, "Colloquium: Topological insulators," Rev. Mod. Phys. **82**, 3045 (2010).

[3] F. D. M. Haldane, "Model for a quantum hall effect without landau levels: Condensed-matter realization of the "parity anomaly"," Phys. Rev. Lett. **61**, 2015 (1988).

[4] F. D. M. Haldane and S. Raghu, "Possible realization of directional optical waveguides in photonic crystals with broken time-reversal symmetry," Phys. Rev. Lett. **100**, 013904 (2008).

[5] Ling Lu, John D. Joannopoulos, and Marin Soljačić, "Topological photonics," Nature Photonics **8**, 821 (2014).

[6] Tomoki Ozawa, Hannah M. Price, Alberto Amo, Nathan Goldman, Mohammad Hafezi, Ling Lu, Mikael C. Rechtsman, David Schuster, Jonathan Simon, Oded Zilberberg, and Iacopo Carusotto, "Topological photonics," Rev. Mod. Phys. **91**, 015006 (2019).

[7] Hosho Katsura, Naoto Nagaosa, and Patrick A. Lee, "Theory of the thermal hall effect in quantum magnets," Phys. Rev. Lett. **104**, 066403 (2010).

[8] Ryuichi Shindou, Ryo Matsumoto, Shuichi Murakami, and Jun-ichiro Ohe, "Topological chiral magnonic edge mode in a magnonic crystal," Phys. Rev. B **87**, 174427 (2013).

[9] V. Peano, C. Brendel, M. Schmidt, and F. Marquardt, "Topological phases of sound and light," Phys. Rev. X **5**, 031011 (2015).

[10] Hussein Nassar, Behrooz Yousefzadeh, Romain Fleury, Massimo Ruzzene, Andrea Alù, Chiara Daraio, Andrew N. Norris, Guoliang Huang, and Michael R. Haberman, "Nonreciprocity in acoustic and elastic materials," Nature Reviews Materials **5**, 667 (2020).

[11] Jean Dalibard, Fabrice Gerbier, Gediminas Juzeliūnas, and Patrik Öhberg, "Colloquium: Artificial gauge potentials for neutral atoms," Rev. Mod. Phys. **83**, 1523 (2011).

[12] N Goldman, G Juzeliūnas, P Öhberg, and I B Spielman, "Light-induced gauge fields for ultracold atoms," Reports on Progress in Physics **77**, 126401 (2014).

[13] Lingzhen Guo, Michael Marthaler, and Gerd Schön, "Phase space crystals: A new way to create a quasienergy band structure," Phys. Rev. Lett. **111**, 205303 (2013).

[14] Yaxing Zhang, J. Gosner, S. M. Girvin, J. Ankerhold, and M. I. Dykman, "Time-translation-symmetry breaking in a driven oscillator: From the quantum coherent to the incoherent regime," Phys. Rev. A **96**, 052124 (2017).

[15] Pengfei Liang, Michael Marthaler, and Lingzhen Guo, "Floquet many-body engineering: topology and many-body physics in phase space lattices," New Journal of Physics **20**, 023043 (2018).

[16] Niels Lörch, Yaxing Zhang, Christoph Bruder, and M. I. Dykman, "Quantum state preparation for coupled period tripling oscillators," Phys. Rev. Research **1**, 023023 (2019).

[17] P. Leboeuf, J. Kurchan, M. Feingold, and D. P. Arovas, "Phase-space localization: Topological aspects of quantum chaos," Phys. Rev. Lett. **65**, 3076 (1990).

[18] P. Leboeuf, J. Kurchan, M. Feingold, and D. P. Arovas, "Topological aspects of quantum chaos," Chaos: An Interdisciplinary Journal of Nonlinear Science **2**, 125 (1992).

[19] Netanel H. Lindner, Gil Refael, and Victor Galitski, "Floquet topological insulator in semiconductor quantum wells," Nature Physics **7**, 490 (2011).

[20] Mark S. Rudner, Netanel H. Lindner, Erez Berg, and Michael Levin, "Anomalous edge states and the bulk-edge correspondence for periodically driven two-dimensional systems," Phys. Rev. X **3**, 031005 (2013).

[21] A. Celi, P. Massignan, J. Ruseckas, N. Goldman, I. B. Spielman, G. Juzeliūnas, and M. Lewenstein, "Synthetic gauge fields in synthetic dimensions," Phys. Rev. Lett. **112**, 043001 (2014).

[22] Tomoki Ozawa and Hannah M. Price, "Topological quantum matter in synthetic dimensions," Nature Reviews Physics **1**, 349 (2019).

[23] Luqi Yuan, Qian Lin, Meng Xiao, and Shanhui Fan, "Synthetic dimension in photonics," Optica **5**, 1396 (2018).

[24] Dominik Suszalski and Jakub Zakrzewski, "Different lattice geometries with a synthetic dimension," Phys. Rev. A **94**, 033602 (2016).

[25] G. M. Zaslavsky, Zakharov M. Yu., R. Z. Sagdeev, D. A. Usikov, and A. A. Chernikov, "Stochastic web and diffusion of particles in a magnetic field," Zh. Eksp. Teor. Fiz. **91**, 500 (1986).

[26] F. L. Moore, J. C. Robinson, C. F. Bharucha, Bala Sundaram, and M. G. Raizen, "Atom optics realization of the quantum δ-kicked rotor," Phys. Rev. Lett. **75**, 4598 (1995).

[27] Julien Chabé, Gabriel Lemarié, Benoît Grémaud, Dominique Delande, Pascal Szriftgiser, and Jean Claude Garreau, "Experimental observation of the anderson metal-insulator transition with atomic matter waves," Phys. Rev. Lett. **101**, 255702 (2008).

[28] Isam Manai, Jean-Fran çois Clément, Radu Chicireanu, Clément Hainaut, Jean Claude Garreau, Pascal Szriftgiser, and Dominique Delande, "Experimental observation of two-dimensional anderson localization with the atomic kicked rotor," Phys. Rev. Lett. **115**, 240603 (2015).

[29] Gabriela B. Lemos, Rafael M. Gomes, Stephen P. Walborn, Paulo H. Souto Ribeiro, and Fabricio Toscano, "Experimental observation of quantum chaos in a beam of light," Nature Communications **3**, 1211 (2012).

[30] G. M. Zaslavsky, Hamiltonian Chaos and Franctional Dynamics (Oxford University Press, Oxford, 2008).

[31] D. J. Wineland, C. Monroe, W. M. Itano, D. Leibfried, B. E. King, and D. M. Meekhof, "Experimental issues in coherent quantum-state manipulation of trapped atomic ions," Journal of research of the National Institute of Standards and Technology **103**, 259 (1998).

[32] Immanuel Bloch, Jean Dalibard, and Wilhelm Zwerger, "Many-body physics with ultracold gases," Rev. Mod. Phys. **80**, 885 (2008).

[33] K. Sacha, "Anderson localization and mott insulator phase in the time domain," Sci. Rep. **5**, 10787 (2015).

[34] Krzysztof Sacha, "Modeling spontaneous breaking of time-translation symmetry," Phys. Rev. A **91**, 033617 (2015).

[35] Lingzhen Guo, Modan Liu, and Michael Marthaler, "Effective long-distance interaction from short-distance interaction in a periodically driven one-dimensional classical system," Phys. Rev. A **93**, 053616 (2016).

[36] Krzysztof Giergiel, Artur Miroszewski, and Krzysztof Sacha, "Time crystal platform: From quasicrystal structures in time to systems with exotic interactions," Phys.

Rev. Lett. **120**, 140401 (2018).
[37] Edward Ott, Chaos in Dynamical Systems (2nd Edition) (Cambridge University Press, The Edinburgh Building, Cambridge CB2 8RU, UK, 2002).
[38] Panagiotis Kotetes, "Classification of engineered topological superconductors," New Journal of Physics **15**, 105027 (2013).
[39] Vittorio Peano, Martin Houde, Christian Brendel, Florian Marquardt, and Aashish A. Clerk, "Topological phase transitions and chiral inelastic transport induced by the squeezing of light," Nature Communications **7**, 10779 (2016).
[40] Charles-Edouard Bardyn, Torsten Karzig, Gil Refael, and Timothy C. H. Liew, "Chiral bogoliubov excitations in nonlinear bosonic systems," Phys. Rev. B **93**, 020502 (R) (2016).
[41] Vittorio Peano and Hermann Schulz-Baldes, "Topological edge states for disordered bosonic systems," Journal of Mathematical Physics **59**, 031901 (2018).
[42] Christian Brouder, Gianluca Panati, Matteo Calandra, Christophe Mourougane, and Nicola Marzari, "Exponential localization of wannier functions in insulators," Phys. Rev. Lett. **98**, 046402 (2007).
[43] Ching-Kai Chiu, Jeffrey C. Y. Teo, Andreas P. Schnyder, and Shinsei Ryu, "Classification of topological quantum matter with symmetries," Rev. Mod. Phys. **88**, 035005 (2016).
[44] C. L. Kane and E. J. Mele, "Quantum spin hall effect in graphene," Phys. Rev. Lett. **95**, 226801 (2005).
[45] B. Andrei Bernevig, Taylor L. Hughes, and Shou-Cheng Zhang, "Quantum spin hall effect and topological phase transition in hgte quantum wells," Science **314**, 1757 (2006).
[46] See Supplemental Material Video for an animation of the time evolution of the topological edge state shown in Fig. 5(a).
[47] K. B. Davis, M. O. Mewes, M. R. Andrews, N. J. van Druten, D. S. Durfee, D. M. Kurn, and W. Ketterle, "Bose-einstein condensation in a gas of sodium atoms," Phys. Rev. Lett. **75**, 3969 (1995).
[48] E. A. Cornell and C. E. Wieman, "Nobel lecture: Bose-Einstein condensation in a dilute gas, the first 70 years and some recent experiments," Rev. Mod. Phys. **74**, 875 (2002).
[49] Daniel Guenther Greif, "Evaporative cooling and bose-einstein condensation of Rb-87 in a moving-coil top trap geometry," Master thesis, (2007).
[50] J. Zak, "Balian-low theorem for landau levels," Phys. Rev. Lett. **79**, 533 (1997).
[51] R. B. Laughlin, "Anomalous quantum hall effect: An incompressible quantum fluid with fractionally charged excitations," Phys. Rev. Lett. **50**, 1395 (1983).
[52] V. J. Goldman, M. Shayegan, and D. C. Tsui, "Evidence for the fractional quantum hall state at $\nu = \frac{1}{7}$," Phys. Rev. Lett. **61**, 881 (1988).
[53] E. Wigner, "On the interaction of electrons in metals," Phys. Rev. **46**, 1002 (1934).
[54] Joonho Jang, Benjamin M. Hunt, Loren N. Pfeiffer, Kenneth W. West, and Raymond C. Ashoori, "Sharp tunnelling resonance from the vibrations of an electronic wigner crystal," Nature Physics **13**, 340 (2017).
[55] Lynn Bonsall and A. A. Maradudin, "Some static and dynamical properties of a two-dimensional wigner crystal," Phys. Rev. B **15**, 1959 (1977).
[56] René Côté and A. H. MacDonald, "Phonons as collective modes: The case of a two-dimensional wigner crystal in a strong magnetic field," Phys. Rev. Lett. **65**, 2662 (1990).
[57] Lingzhen Guo and Pengfei Liang, "Condensed matter physics in time crystals," New Journal of Physics **22**, 075003 (2020).
[58] Lingzhen Guo, Vittorio Peano, and Marquardt Florian, in preparation.
[59] T. P. Billam and S. A. Gardiner, "Quantum resonances in an atom-optical δ-kicked harmonic oscillator," Phys. Rev. A **80**, 023414 (2009).
[60] Belén Paredes, Artur Widera, Valentin Murg, Olaf Mandel, Simon Fölling, Ignacio Cirac, Gora V. Shlyapnikov, Theodor W. Hänsch, and Immanuel Bloch, "Tonks-girardeau gas of ultracold atoms in an optical lattice," Nature **429**, 277 (2004).
[61] Henning Moritz, Thilo Stöferle, Michael Köhl, and Tilman Esslinger, "Exciting collective oscillations in a trapped 1d gas," Phys. Rev. Lett. **91**, 250402 (2003).
[62] Zoran Hadzibabic, Sabine Stock, Baptiste Battelier, Vincent Bretin, and Jean Dalibard, "Interference of an array of independent bose-einstein condensates," Phys. Rev. Lett. **93**, 180403 (2004).